SANDIA REPORT

SAND2014-18411
Unlimited Release
Printed September 2014

Verification and Validation of Carbon-Fiber Laminate Low Velocity Impact Simulations

Shawn A. English
Stacy M. Nelson
Timothy M. Briggs
Arthur A. Brown

Prepared by
Sandia National Laboratories
Albuquerque, New Mexico 87185 and Livermore, California 94550

Sandia National Laboratories is a multi-program laboratory managed and operated by Sandia Corporation, a wholly owned subsidiary of Lockheed Martin Corporation, for the U.S. Department of Energy's National Nuclear Security Administration under contract DE-AC04-94AL85000.

Issued by Sandia National Laboratories, operated for the United States Department of Energy by Sandia Corporation.

Available to DOE and DOE contractors from
U.S. Department of Energy
Office of Scientific and Technical Information
P.O. Box 62
Oak Ridge, TN 37831

Telephone: (865) 576-8401
Facsimile: (865) 576-5728
E-Mail: reports@adonis.osti.gov
Online ordering: http://www.osti.gov/bridge

Available to the public from
U.S. Department of Commerce
National Technical Information Service
5285 Port Royal Rd.
Springfield, VA 22161

Telephone: (800) 553-6847
Facsimile: (703) 605-6900
E-Mail: orders@ntis.fedworld.gov
Online order: http://www.ntis.gov/help/ordermethods.asp?loc=7-4-0#online

SAND2014-18411
Unlimited Release
Printed September 2014

Verification and Validation of Carbon-Fiber Laminate Low-Velocity Impact Simulations

Shawn A. English
Stacy M. Nelson
Timothy M. Briggs
Arthur A. Brown
Sandia National Laboratories
P.O. Box 969
Livermore, CA 94551-0969

Abstract

Presented is a model verification and validation effort using low-velocity impact (LVI) of carbon fiber reinforced polymer laminate experiments. A flat cylindrical indenter impacts the laminate with enough energy to produce delamination, matrix cracks and fiber breaks. Included in the experimental efforts are ultrasonic scans of the damage for qualitative validation of the models. However, the primary quantitative metrics of validation are the force time history measured through the instrumented indenter and initial and final velocities. The simulations, which are run on Sandia's Sierra finite element codes, consist of all physics and material parameters of importance as determined by a sensitivity analysis conducted on the LVI simulation. A novel orthotropic damage and failure constitutive model that is capable of predicting progressive composite damage and failure is described in detail and material properties are measured, estimated from micromechanics or optimized through calibration. A thorough verification and calibration to the accompanying experiments are presented. Special emphasis is given to the four-point bend experiment. For all simulations of interest, the mesh and material behavior is verified through extensive convergence studies. An ensemble of simulations incorporating model parameter uncertainties is used to predict a response distribution which is then compared to experimental output. The result is a quantifiable confidence in material characterization and model physics when simulating this phenomenon in structures of interest.

CONTENTS

FIGURES

TABLES

NOMENCLATURE

CDM	Continuum Damage Mechanics
CFRP	Carbon Fiber Reinforced Polymer
PMC	Polymer Matrix Composite
LVI	Low-Velocity Impact
NDE	Non-destructive Evaluation
CT	Computed Tomography
CNC	Computer Numerical Control
RDE	Relative Discretization Error
ANOVA	Analysis of Variance
FEA	Finite Element Analysis
CZ	Cohesive Zone
FCT	Feature Coverage Tool
PERT	Phenomena Identification Ranking Table
PCMM	Predictive Capability Maturity Model
WSEAT	Weapons Systems Engineering Assessment Technology

1. INTRODUCTION

Verification and validation are essential elements for the qualification of numerical models, in other words building quantifiable confidence in simulation results. The definition we will use for validation is [1]: "The process of determining the degree to which a computer model is an accurate representation of the real world from the perspective of the intended model applications". Each input of the model adds a degree of freedom, making identifying the highly contributing inputs difficult. To remedy this, a sensitivity analysis is conducted prior to the implementation of a validation analysis. In this case, a validation analysis refers to a sampling over all input distributions to produce a single distribution of response metrics from which both a statistical judgment is made on validity as well as an estimate of uncertainty. A sensitivity analysis utilizes a design of experiments method to isolate the effect of each input relative to other inputs. The applications of parametric sensitivity analyses have proven to be fairly far reaching with sampled references demonstrating relationships to many different scientific fields [2-7]. For the purposes of this study, the sensitivity analysis will be used to determine which of the material inputs are most critical to predictions of failure and uncertainty quantification will be used to propagate any input parameter unknowns through to the predicted output response.

With the results of the sensitivity analysis, extensive material characterization efforts are carried out with limited experimental data. Independent experiments, such as the four-point bending, are used for calibration of various inputs. Other parameters are measured, estimated from micromechanics [8, 9], found in literature or estimated with engineering judgment.

Verification of the model and code is done through mesh convergence studies and regression tests for most of the physics present in the model (i.e. contact, constitutive models, element formulation, etc.). The laminate material model was generated in conjunction with this study, so verification was completed on the theoretical formulation by subject matter experts and numerical output using various representative simulations, such as single element, implicit quasi-static and explicit dynamic crack growth for mesh sensitivities.

This work documents a simplified verification and validation effort for the low-velocity impact (LVI) modeling of carbon fiber reinforced composite. In the case of LVI with post-test non-destructive evaluation (NDE), quantitative as well as qualitative assessment is necessary. While the residual strength is untested in both experiments and model, the qualitative metrics such as crack length and depth, delaminated area and quasi-quantitative metrics such as load time shape are an important way to assess relevant engineering statistics. However, an overall qualification metric must be quantifiable and contain sensitivities to many of the input parameters. Calibration, or the adjustment of model inputs in order to match the experimental response, is completed to prove deficiencies in the model and direct future efforts. The primary metric for comparison is the loss of kinetic energy calculated from initial and rebound velocities of the indenter fixture. The experiments are conducted on a 12 layer 8 harness carbon reinforced polymer. The material is minimally characterized, leaving many model inputs unknown. The force time histories and pre- and post-impact ultrasonic scans are utilized as validation metrics.

2. EXPERIMENTATION

2.1. Material Description

The carbon fiber reinforced polymer (CFRP) material was used for this investigation consisting of an 8-harness satin weave prepreg with an epoxy based resin. Laminates were hand layed up from precut ply kits using a CNC controlled ply cutter to control geometry and orientation. The fiber volume fraction was approximately 48% and the material was cured in the form of flat plates using a standard autoclave process under vacuum at 350° F and 45 psig of pressure. Specimens were then cut from consolidated laminates using a wet diamond saw to the dimensions shown in Table 1 and Table 2. For the textile architecture used in this study, one ply is denoted as (0/90) representing the warp and fill directions in the 0° and 90° directions, respectively. Therefore, the laminates used in this investigation were composed of 12 plies of textile material with the warp direction oriented along the specimen's length.

Table 1: Typical dimensions for impact specimens

Width (mm)	Length (mm)	Thickness (mm)	Stack Sequence
102	*155*	*4.49*	$[(0/90)_6]_s$

Table 2: Typical dimensions for flexural specimens

Width (mm)	Length (mm)	Thickness (mm)	Stack Sequence
24.6	*135*	*2.95*	$[(0/90)_6]_s$

2.2. Test Setup

2.2.1. Four point bend

The described specimens were tested to failure in 4-point flexure under displacement control with the conditions described in Table 3 and illustrated in Figure 6. During each test, displacement and load data was recorded directly from the testing machine crosshead and load cell with an acquisition rate of 10 Hz.

Table 3: Four-point flexure testing conditions

Support Span (mm)	Loading Span (mm)	Displacement Rate (mm/min)
100	*50*	*5.0*

Upon testing completion, the measured specimen dimensions and recorded load-displacement data were used to determine the flexural stress and strain as well as the flexural modulus. For this

four point loading configuration, the maximum displacement and the crosshead displacement differences are accounted for, allowing the strain, ε, and flexural modulus, E_f, to be expressed as:

$$\varepsilon = \frac{6t}{L^2} V_c \tag{1}$$

$$E_f = \frac{L^3}{8wt^3}\left(\frac{P}{V_c}\right) \tag{2}$$

where the thickness, t, width, w, and length, L, are all specified from the specimen geometry, and the crosshead displacement, V_c, and applied load, P, are directly measured during the experiment. The flexural stress, σ_f, can be computed from equations (1) and (2), and is independent of the crosshead displacement. Also, the stiffness of the load frame and fixturing was taken into account with respect to the flexural rigidity of the specimen, allowing the crosshead displacement to be used in all calculations rather than a direct measure of the central span deflection, simplifying the procedure.

2.2.2. Low-Velocity Impact

A gravity accelerated drop weight impact tester was used to perform instrumented impact experiments on the flat specimens, as shown in Figure 1. Below the pin located flat specimen there was an unsupported central region approximately 76 mm by 127 mm, corresponding to the width and length directions of the specimen, respectively. The specimen was not securely clamped, rather a pair of toggle clamps was closed to the point that they constrained any vertical displacement of the specimen edges. The incident kinetic energy of impact was controlled with the mass of the crosshead and its drop height, set at 50 J and 25 J for this investigation. The impact tip was a 19 mm diameter cylinder with a flat face made of stainless steel. The impact experiment was conducted by adjusting the drop height appropriately for the mass of the crosshead in order to achieve the desired energy level, as detailed in Table 4. A light sensor was used to determine the initial velocity just prior to impact in order to perform necessary integration of the acceleration response obtained from the dynamic load cell. The subsequent integration of the directly measured force response allowed velocity, deflection and energy calculations during the impact event. The force response was filtered at 12 kHz and data was collected at a frequency of approximately 820 kHz for the entire duration of the impact event. The rebound velocity was determined as the crosshead passed through the light sensor a second time on its way back up off the specimen. Rebound brakes were then activated preventing a second impact event onto the specimen.

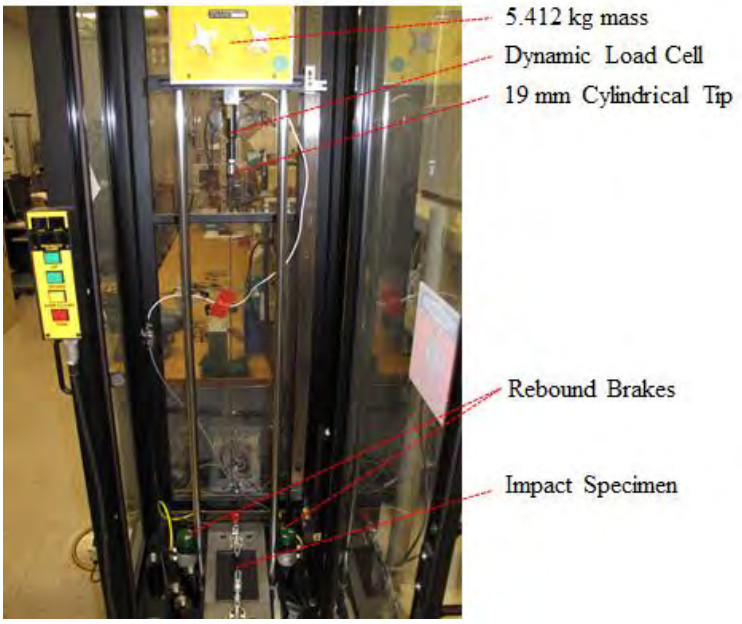

Figure 1: Impact test setup showing main components

Table 4: Low-velocity impact testing conditions

Impact Energy	Crosshead Mass	Impact Velocity
50 J	*5.412 kg*	*4.3 m/s*

In order to visualize, measure and delineate between damage form and location, pre- and post-impact specimens were both ultrasonically scanned and imaged with 3-dimensional computed tomography (CT). Ultrasonic scanning was performed using a 5 MHz transducer with a focal length of 2 inches with specimens submerged in water to act as a coupling agent. All specimens were adequately baked out after water exposure before mechanical testing. CT scanning was performed using a 225 KeV energy level and a target power of 54 W.

3. FINITE ELEMENT MODEL

3.1. Model Description

The finite element mesh, shown in Figure 2, consists of the lower impactor geometry, a lumped mass, a fixed holder to represent the toggle clamps, the base and the specimen. The experiments consistently showed crack preference towards one side of the test fixture; indicating skew impact of the tup on the specimen. This angle of impact was measured as 0.45^0. Since this error was only observed on one of the principal axes, the model is half symmetric.

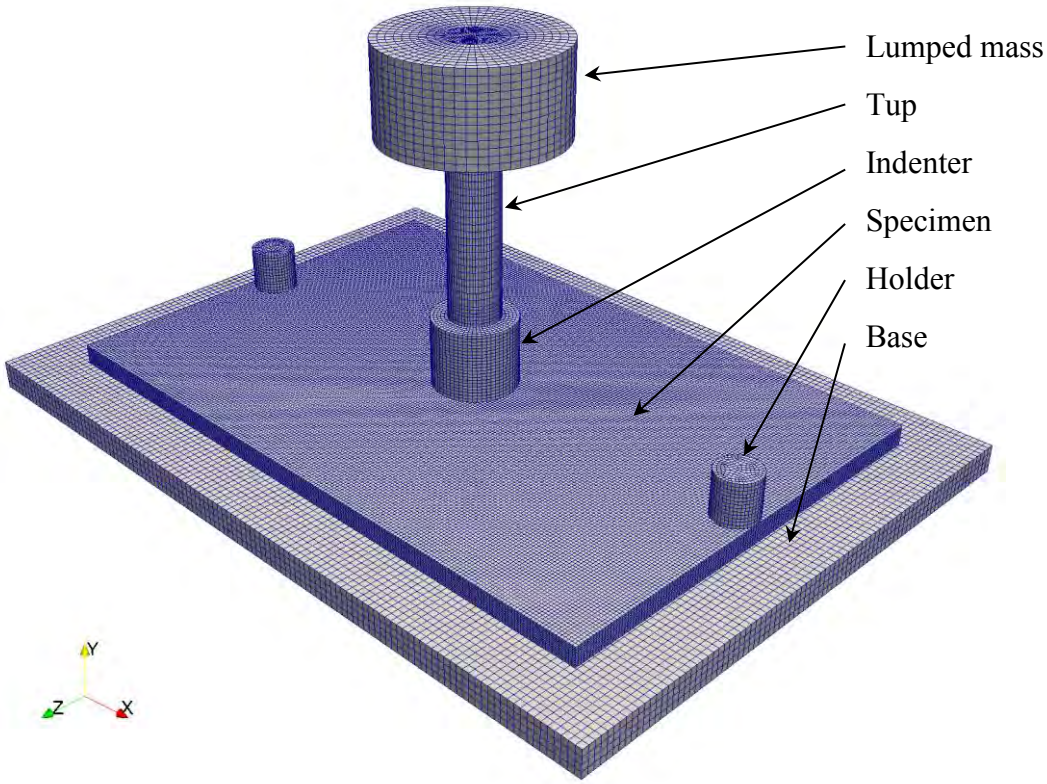

Figure 2: Full mesh of simulated low velocity impact experiment (note: x-plane symmetry is utilized)

3.2. Verification

3.2.1. Code Verification

Code verification is completed via nightly regression tests and other means to ensure there are no errors in the numerical computation. The feature coverage tool (FCT) is utilized to assess the code testing. The FCT indicates 74% of the features are verified individually and 82% are tested nightly. However, the two way coverage of code verification is quite dismal at 27%. Figure B-1

shows the two-way coverage results. The material models are deemed the most critical in terms of verified functionality. Each material model used in this study is tested within the code with at least one-way coverage.

3.2.2. Mesh Convergence

This section will address solution verifications or the assessment of errors associated with discretization of the problem. First the discretization error is estimated through mesh convergence studies on all finite element models of interest. The order of mesh convergence is given for a uniform mesh refinement factor *r* and metrics for each mesh refinement *f,* is given as

$$p = \frac{ln\left(\frac{f_3 - f_1}{f_2 - f_1}\right)}{ln(r)} \tag{3}$$

Then the relative discretization error is estimated by

$$RDE = \frac{f_k - f_{exact}}{f_{exact}} \tag{4}$$

Where the exact value is estimated from Richardson's extrapolation as

$$f_{exact} \approx f_1 + \frac{f_1 - f_2}{r^p - 1} \tag{5}$$

While possible for small applications, numerical limitations prevent the use of more than one element per lamina. Similarly, the aspect ratio (in-plane versus out-of-plane) of the elements must be large enough to limit degrees of freedom in the mesh. Therefore, uniform mesh refinements result in multiple layers through the thickness per element. Since the damage model can identify out-of-plane failure and the material is assumed homogenized through the thickness, the mesh convergence study works backwards from the 12 elements through the thickness model uniformly. The meshes are as follows: 3, 6 and 12 elements through the thickness with an element aspect ratio of 2, corresponding to characteristic element sizes of l^* = 0.37, 0.75 and 1.50 mm respectively. The coarsest mesh forced an artificial toughness increase to accommodate the larger characteristic length. This was completed for all the mesh convergence models and therefore should not have an effect on the relative results.

It should be noted that crack initiation force (first peak) in the LVI simulations is mesh sensitive due to the presence of a the sharp edged indenter. While the proper method to alleviate this sensitivity is to model the fillet on the indenter, this feature is smaller than the homogenization length of the lamina. In this case, fracture initiation is no longer associated with the homogenized material response over the length of the representative volume element. Therefore, the energy absorbed due to fracture, while not independent of this limitation, should be a suitable homogenized response metric. Figure 3 shows the %RDE of energy dissipated for three mesh refinements. The characteristic length is defined by the mesh size, or the length over which the distributed cracks are homogenized. The finest element sized (l^* = 0.37 mm) is necessary for the

validation simulations, while computational constraints forced using an aspect ratio of 4 with 12 elements through the thickness for the sensitivity analysis.

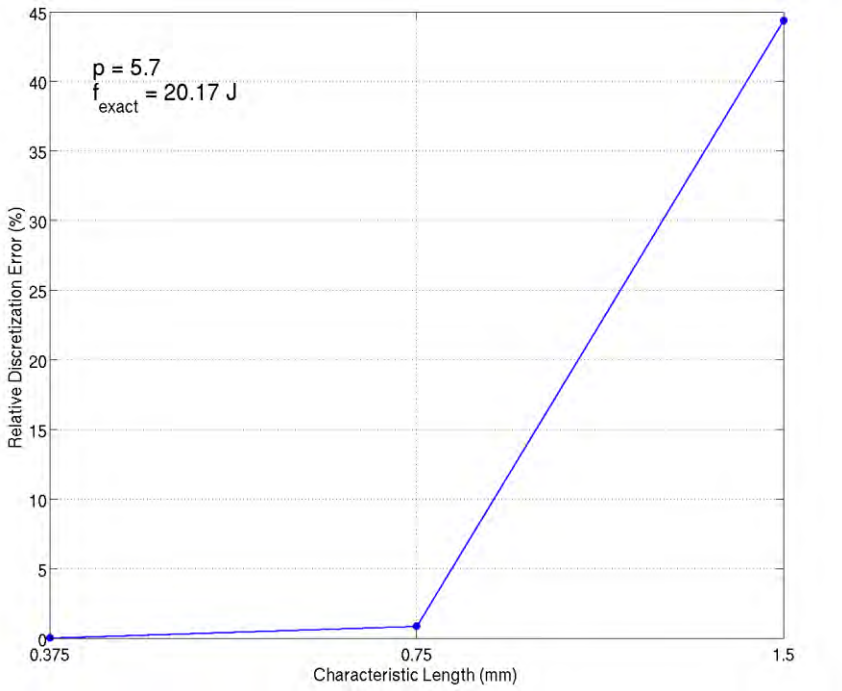

Figure 3: Percent RDE of energy dissipated for three mesh refinements

The convergence study on mesh size confirms a mesh size small enough to capture shear cracking at the point of impact produces converging results with decreasing mesh size. This is a result of the delamination, which is the primary mode of failure, being mesh insensitive at these sizes. The final mesh consists of 1.1 million reduced integration hexahedral elements. As a result of the composite failure constitutive model formulation, mesh convergence does not indicate mesh independence since the mesh size is an input.

3.2.3. Geometric Sensitivity

Three major assumptions are made in the geometric representation of the experiment. First, the indenter, tup (shaft) and mass are assumed solid and contiguous. Similarly, the instrumented tup compliance does not affect the solution. Second, the total mass of the guide assembly and weights are represented with a single cylinder with an artificial density and is fixed at the mid-plane in the direction of the guides (*z*-axis). Third, the holder preload and geometry are accurately represented by rubber cylinders fixed at the top with no preload. While the effect of the presence of the holder is evaluated, only the sensitivity to the tup compliance is assessed here. Figure 4 shows three force time histories for three moduli of the instrumented tup, with soft, medium and hard at E = 34.5, 68.9 and 137.8 GPa respectively; The resulting energy absorptions are 20.8, 21.2, and 20.6 J for the soft, medium and hard respectively. The frequency

and amplitude in the force oscillations and the energy absorbed are sensitive to the modulus. However, the energy absorbed response seems to be random. Moreover, calibrating to the experimental data is not possible due to filtering. One option would be to estimate the effective modulus through modeling or experiments. However, this was not completed for this study. Using only engineering judgment, the modulus corresponding to aluminum is used for the validation runs.

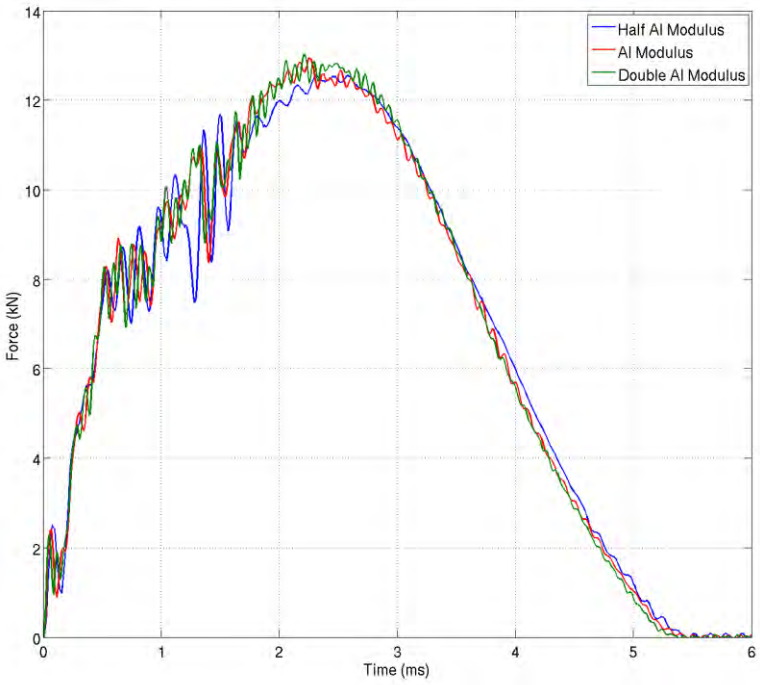

Figure 4: Force versus time for three tup moduli

3.3. Sensitivity Analysis

Prior to the completion of any simulations predicting a loaded composite's structural response, a complete sensitivity analysis can be used to determine which of the material model input parameters are most influential to the simulated response. Then, at a minimum, only those influential material input parameters need to be defined through careful experimental characterization.

As will be discussed in the ensuing sections, an orthotropic-elastic-failure model, which requires the definition of 77 separate material input parameters, was developed for this study. This number of parameters is difficult to determine through experimental characterization. Rather, a sensitivity analysis can be applied to determine which of those 77 parameters are truly influential to the simulated response, and then only those critical parameters must be defined rigorously.

As a first step, prior to initializing the sensitivity study, engineering judgment can be used to eliminate any of the 77 parameters intuitively insignificant to a specific load case of interest. Then, with the remaining k parameters, a set of computer experiments can be designed in which the k-dimensional parameter space is sampled numerous times and each sampled parameter set is applied to a structural simulation utilizing a deterministic code, such as Sierra Adagio. Furthermore, if the high-dimensional parameter space is sampled in a representative, or organized, fashion, a minimum number of sample sets and simulations can be used to develop and recognize trends and relationships between the individual k input parameters and the simulated output.

There are many different approaches that can be taken to efficiently sample the k-dimensional parameter space. One such approach is the Box Behnken Design method (BBD). This approach, which was chosen for all ensuing sensitivity studies, offers a highly stable sampling method. Specifically, the BBD methodology avoids overtly extreme parameter combination in which all factors are simultaneously at their highest or lowest values. Furthermore, although the Box-Behnken methodology samples at the bounds of the parameter space, unlike similar methods (e.g. central composite design method), the BBD method does not sample outside of the process space. Figure 5 represents the process space corresponding to three critical parameters, or $k = 3$. As shown in the figure, an average, minimum, and maximum value is defined for each of the three variables. Visually, the minimum and maximum values occur at the edges of planes representing the different parameters and the average values correspond to the shared origin. The Box Behnken Design method samples this three-dimensional parameter space systematically by increasing or decreasing two variables from their means to the extrema and holding all other variables at their averages.

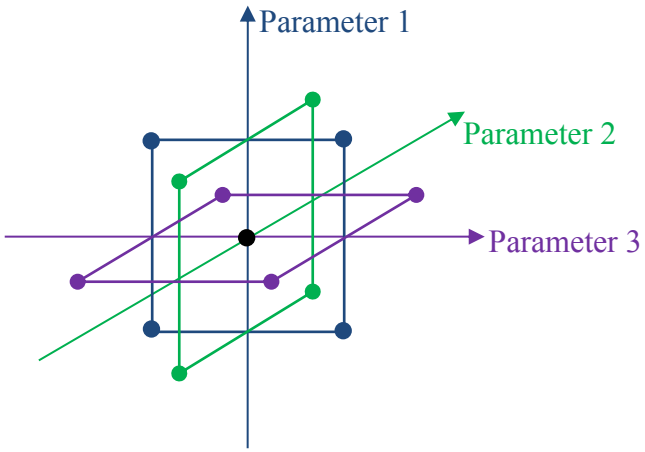

Figure 5: Box Behnken parameter space corresponding to three variables (k = 3)

In addition to improved stability, when compared to other similar approaches, the Box Behnken method also seems to require fewer overall samples to develop trends between the input parameters and the output. The relationship between the number of computer experiments designed with the BBD approach and k input parameters can be expressed as:

$$N = 2k(k-1) + 1 \tag{6}$$

where N is the number of experiments, or simulations, designed and k is the number of parameters [10].

Upon completion of the N simulations, the individual parameter sensitivities can be assessed. This assessment can be readily conducted with a multi-way analysis of variance (ANOVA). Specifically, the ANOVA represents a model independent, probabilistic sensitivity analysis method that can be used to determine the existence of statistical associations between an output response and one or more input parameters [11].

Within a multi-variable analysis there is a single response variable that is dependent upon multiple "factor" variables, or design parameters. These design parameters can take on any number of numerical values, or "levels," and the resulting factor-level combinations are known as "cells." With this in mind, the response variable, or model output, associated with a given cell combination, can be thought of as the summation of a cell mean and an error term, which is represented below in Equation (7) for a two-factor analysis.

$$Y_{ijk} = \mu_{ij} + E_{ijk} \tag{7}$$

Where:
- Y: the response variable
- μ: the cell mean
- E: the error/residual term
- i: level of factor 1
- j: level of factor 2
- k: kth observation within the ij cell

The ANOVA provides an estimation of the cell mean, which in turn can be used to determine the error, or residual, term. This is specifically achieved through the decomposition of the observation data's variance into the associated sum of squares components. Equations (8) through (12) represent these components for a two-factor analysis.

Sum of squares for factor 1:
$$\mathrm{rb}\sum_{i=1}^{a}(\bar{y}_{i\cdot\cdot} - \bar{y}_{\cdot\cdot\cdot})^{2} \tag{8}$$

Where:
- r: number of observations within ij cell
- b: number of factor 2 levels
- a: number of factor 1 levels
- $\bar{y}$: mean of the indicated observations

Sum of squares for factor 2:
$$\mathrm{ra}\sum_{j=1}^{b}(\bar{y}_{\cdot j\cdot} - \bar{y}_{\cdot\cdot\cdot})^{2} \tag{9}$$

Sum of squares of factor 1/2 interaction:
$$\sum_{i=1}^{a}\sum_{j=1}^{b}(\bar{y}_{ij\cdot} - \bar{y}_{i\cdot\cdot} - \bar{y}_{\cdot j\cdot} - \bar{y}_{\cdot\cdot\cdot})^{2} \tag{10}$$

Sum of squares of the error/residual:

$$\sum_{k=1}^{r}\sum_{j=1}^{b}\sum_{i=1}^{a}(\bar{y}_{ijk}-\bar{y}_{ij\cdot})^{2} \tag{11}$$

Total sum of squares:

$$\sum_{k=1}^{r}\sum_{j=1}^{b}\sum_{i=1}^{a}(\bar{y}_{ijk}-\bar{y}_{\cdots})^{2} \tag{12}$$

Next, the sum of squares components can be used to determine the data's mean square values. Equations (13) through (16) represent these values for a two-factor analysis:

Mean square for factor 1:

$$\frac{sum\ of\ squares\ for\ factor\ 1}{a-1} \tag{13}$$

Mean square for factor 2:

$$\frac{sum\ of\ squares\ for\ factor\ 2}{b-1} \tag{14}$$

Mean square of factor 1/2 interaction:

$$\frac{sum\ of\ squares\ of\ interaction}{(a-1)(b-1)} \tag{15}$$

Mean square of the error/residual:

$$\frac{sum\ of\ squares\ of\ residual}{(total\ \#\ of\ observations-1)-[(a-1)+(b-1)]} \tag{16}$$

Then, the mean square values can be used to determine the "F-statistic," which is relevant in the determination of the significance of any individual design parameter to the model's output response. The F-statistic should be determined for each factor as well as for every possible factor interactions, as it is possible the individual factors may be significant to the output and not their interactions and vice versa:

F-statistic of factor/interaction:

$$\frac{mean\ square\ of\ factor\ or\ interaction}{mean\ square\ of\ residual} \tag{17}$$

Lastly, the calculated F-statistic values can be compared with published critical values of F to determine any specific sensitivities within a given parameter space.

Some material parameters are estimated with micro-mechanics and others using literature of the same or similar material. In the end, engineering judgment is often employed to set bounds for uniform distributions. From this analysis, the obvious parameters, such as the in-plane stiffnesses and mode II interlaminar fracture toughness, are determined influential on the response. Additionally, the friction coefficient and out-of-plane shear properties are determined significant; indicating further investigation and experimental data is necessary. For this study,

these significant parameters will serve as a basis for error assessment and model adjustment subsequent to validation analysis.

In the LVI simulations, the total number of runs necessary to sample over 52 inputs is 5305. Due to the high number of runs, a coarser mesh was necessary. The coarse model under predicts the energy dissipated and can produce questionable mechanisms of failure.

3.4. Materials

3.4.1. Elastic Orthotropic Failure

An elastic orthotropic damage evolution and failure material model is developed for this study. The formulation follows closely with [12-14]. Crack band theory is implemented, where distributed crack growth is assumed through a localization event. Prior to softening, distributed damage is allowed to evolve in the element resulting in a "hardening" stress strain response. Failure, or crack localization, is assumed to be distributed across the crack band and softening is controlled by size-dependent fracture energy [15]. Since elastic damage is assumed to be the only source of stiffness loss, damage variables can be introduced for each of the normal and shear components of stress. The corresponding compliance tensor takes on the following form [12]:

$$\mathbf{S} = \begin{bmatrix} \frac{1}{E_{11}(1-d_{11})} & \frac{-\upsilon_{21}}{E_{22}} & \frac{-\upsilon_{31}}{E_{33}} & 0 & 0 & 0 \\ \frac{-\upsilon_{12}}{E_{11}} & \frac{1}{E_{22}(1-d_{22})} & \frac{-\upsilon_{32}}{E_{33}} & 0 & 0 & 0 \\ \frac{-\upsilon_{13}}{E_{11}} & \frac{-\upsilon_{23}}{E_{22}} & \frac{1}{E_{33}(1-d_{33})} & 0 & 0 & 0 \\ 0 & 0 & 0 & \frac{1}{2G_{12}(1-d_{12})} & 0 & 0 \\ 0 & 0 & 0 & 0 & \frac{1}{2G_{13}(1-d_{13})} & 0 \\ 0 & 0 & 0 & 0 & 0 & \frac{1}{2G_{23}(1-d_{23})} \end{bmatrix} \tag{18}$$

The damaged (actual) stresses and strains are

$$\sigma_{ij} = C_{ijkl}\varepsilon_{kl} \tag{19}$$

$$\varepsilon_{ij} = S_{ijkl}\sigma_{kl} \tag{20}$$

where

$$C_{ijkl} = S_{ijkl}^{-1} \tag{21}$$

Since the compliance tensor becomes singular at $d = 1$, the stiffness tensor is written in closed form where the limit of stiffness as $d \rightarrow 1$ exists.

A quadratic strain criterion is used for damage initiation and failure. The damage activation threshold is evaluated for tension and compression, matrix and fiber modes and for each of the primary material planes [13, 14, 16]. The damage activation function for the matrix mode in the 11 plane is given for tension and compression as

Tension:
$$\varphi_{11+}^{m} = \sqrt{\left(\frac{E_{11}\langle\varepsilon_{11}\rangle}{X_{11+}^{m}}\right)^2 + \left(\frac{G_{12}\gamma_{12}}{S_{12}^{m}}\right)^2 + \left(\frac{G_{13}\gamma_{13}}{S_{13}^{m}}\right)^2} \tag{22}$$

Compression:
$$\varphi_{11-}^{m} = \sqrt{\left(\frac{E_{11}\langle-\varepsilon_{11}\rangle}{X_{11-}^{m}}\right)^2 + \left(\frac{G_{12}\gamma_{12}}{S_{12}^{m}}\right)^2 + \left(\frac{G_{13}\gamma_{13}}{S_{13}^{m}}\right)^2} \tag{23}$$

where $\langle\ \rangle$ are the Macaulay brackets, defined as

$$\langle x\rangle = \begin{cases} 0, & x < 0 \\ x, & x \geq 0 \end{cases} \tag{24}$$

The user provides only damage initiation/failure stresses (X^f). For failure in the fiber mode the stress used in the damage activation function must be the effective stress. For strain equivalency, the effective strength in the 11 direction is simply

$$\bar{X}^f = E_{11}\varepsilon_{11}^f \tag{25}$$

where ε_{11}^f is the strain to fiber failure. Therefore, the damage activation function for the fiber mode in the 11 plane is given for tension and compression as

Tension:
$$\varphi_{11+}^{f} = \sqrt{\left(\frac{E_{11}\langle\varepsilon_{11}\rangle}{\bar{X}_{11+}^{f}}\right)^2 + \left(\frac{G_{12}\gamma_{12}}{\bar{S}_{12}^{f}}\right)^2 + \left(\frac{G_{13}\gamma_{13}}{\bar{S}_{13}^{f}}\right)^2} \tag{26}$$

Compression:
$$\varphi_{11-}^{f} = \sqrt{\left(\frac{E_{11}\langle-\varepsilon_{11}\rangle}{\bar{X}_{11-}^{f}}\right)^2 + \left(\frac{G_{12}\gamma_{12}}{\bar{S}_{12}^{f}}\right)^2 + \left(\frac{G_{13}\gamma_{13}}{\bar{S}_{13}^{f}}\right)^2} \tag{27}$$

The user specified fracture energy for a given mode of failure is the total energy associated with material bifurcation in this mode. The current model formulation does not account for mixed mode coupling during fracture.

Crack band theory assumes that a band of continuously distributed parallel cracks [15] produces the same energy released as line crack. The opening stress to relative displacement (δ) relationship is therefore replaced with the presumed identical $\delta = \varepsilon l^*$, where, l^* is the characteristic length of the finite element and ε is the homogenized strain in the crack opening direction [14].

Damage evolution is user defined only for matrix mode failure. The evolution of fiber damage is controlled by internal parameters using the fracture energies and crack band theory. For each matrix failure mode (tension, compression, shear), the evolution equation is generally defined as

$$d = 1 - \frac{K_m}{E} + \left(\frac{K_m}{E} - 1\right)\frac{1}{r_m^n} \tag{28}$$

where K_m and n are the matrix mode damage modulus and exponent respectively. The damage exponent is intended to add flexibility in the material response. For shear damage, K_m is defined in τ - γ space. After the fiber mode strength is exceeded, the material is linearly softened. Note matrix mode damage is zero for $K_m = E$ or $n = 0$.

3.4.2. Cohesive Zone Traction Separation Law

For a model with at least one element through the thickness per lamina each interface is modeled as a plane separated by cohesive zone (CZ) zero volume hexagonal elements. A simple mixed-mode traction separation law detailed in [17] is used for delamination prediction. Interpenetration is prevented with contact definition. This precaution is necessary to prevent layer interpenetration after cohesive element failure. A benefit of this technique is the appearance of compression dependent mode II peak traction and thus toughness similar to [18]. Therefore, for a constant normal stress (σ_n), the effective peak traction and toughness are simply

$$\tau^* = \tau + \mu\langle -\sigma_n \rangle \tag{29}$$

$$G_{II}^* = G_{II} + \mu\delta_{TC}\langle -\sigma_n \rangle \tag{30}$$

where μ is the frictional coefficient and δ_{TC} is the critical tangential separation. Since after element failure a frictional interface is assumed, the current model cannot differentiate surfaces enclosing a failed element, i.e. a single friction coefficient controls both CZ traction and frictional forces. The model form is known to be in error in this regard.

3.5. Material Characterization and Calibration

3.5.1. Cohesive Zone Traction Separation Law

Mode I and mode II interlaminar toughness predictions for the cohesive element characterization come from double cantilever beam and end notch flexure experiments respectively. The failure model is complex and requires an extensive experimental program to characterize. In-plane tensile properties are measured directly from experiments. Some properties, such as the in-plane compressive strength, are calibrated to experiments that exhibit a specific phenomenon of interest. Other properties are estimated from literature or calculated through micromechanical simulations. Properties not directly measured are given bounds, thus assuming a uniform distribution between two likely extrema. Each measured property is either applied directly and verified or calibrated to match experiments.

Verification of the end notched flexure experiments proved challenging. The crack initiation toughness in the models needed to be lower than the calculated toughness from the experiments in order to produce similar peak loads. Instead, the experimentally determined energy dissipated over the measured crack area (average fracture toughness) was used as the toughness for the cohesive zone model, which led to higher peak loads. The discrepancies in the load displacement curves are likely caused by mechanisms such as fiber bridging and initial crack bluntness that are not explicitly captured in the model. Therefore, rather than calibrating to experimental load versus displacement, the toughness values used in the model are calculated from experimental data. Calibrating "frictional" method of compression sensitivity, was not complete. Conservative values were used in order to provide some level of effectiveness. The actual level of mode II toughness sensitivity on compressive stress is likely higher, as seen in [19].

Table 5: Interlaminar material properties

Identification	Values
G_I (J/m^2)	282 (45)
G_{II} (J/m^2)	782 (87)
μ	0.45 ± 0.25
σ_0 (MPa)	10 ± 1.0
τ_0 (MPa)	32.4± 7.4

3.5.2. Elastic Orthotropic Failure

The properties for the 8HS CFRP are shown in Table 6. Standard deviations are given in parentheses and bounds of uniform distributions are shown as ±. Very large ranges are often utilized in the sensitivity analysis due to lack of decent predictions. Once deemed influential, the parameters are better estimated.

Table 6: CFRP material properties

Identification	Values	Identification	Values
E_{11} (GPa)	63.9 (2.4)	F_{1T} (MPa)	769 (37)
E_{22} (GPa)	62.7 (3.8)	F_{1C} (MPa)	816 (69)
E_{33} (GPa)	8.19 ± 0.40	F_{2T} (MPa)	823 (26)
v_{12}	0.048 (0.018)	F_{2C} (MPa)	816 (69)
v_{23}	0.399 ± 0.018	F_{3T} (MPa)	56.2 ± 13
v_{13}	0.400 ± 0.017	F_{3C} (MPa)	56.2 ± 13
G_{12} (GPa)	3.44 (0.058)	S_{12M} (MPa)	48.4 (0.84)
G_{23} (GPa)	3.27 ± 0.27	S_{12F} (MPa)	77.3 (1.1)
G_{13} (GPa)	3.25 ± 0.26	S_{23M} (MPa)	32.4 ± 7.4
G_{I11}	80 ± 20	S_{23F} (MPa)	65.5 ± 12
G_{I22}	80 ± 20	S_{13M} (MPa)	32.4 ± 7.4
G_{I33}	2.6 ± 2.5	S_{13F} (MPa)	65.5 ± 12
G_{III2}	12 ± 1.2	K_{12m} (MPa)	152 (10.1)
G_{II23}	10 ± 1.0	K_{23m} (MPa)	152 ± 15.2
G_{II13}	10 ± 1.0	K_{13m} (MPa)	152 ± 15.2

4. RESULTS

4.1. Experimental Results

4.1.1. Four-point Bend

Each of the tested specimens was evaluated for the maximum stress and strain values in the outer plies. These values were calculated with classical elasticity theory and plotted in order to identify the characteristic features such as initial softening and flexural failure. As can be seen in Figure 6, a typical load-time response is illustrated with respective images detailing the events at each relevant point in time. The sequence from A through C will be the focus of this investigation, highlighting the initial softening and 'failure.' The subsequent sequence of events is beyond the scope of the modeling effort and included only for completeness.

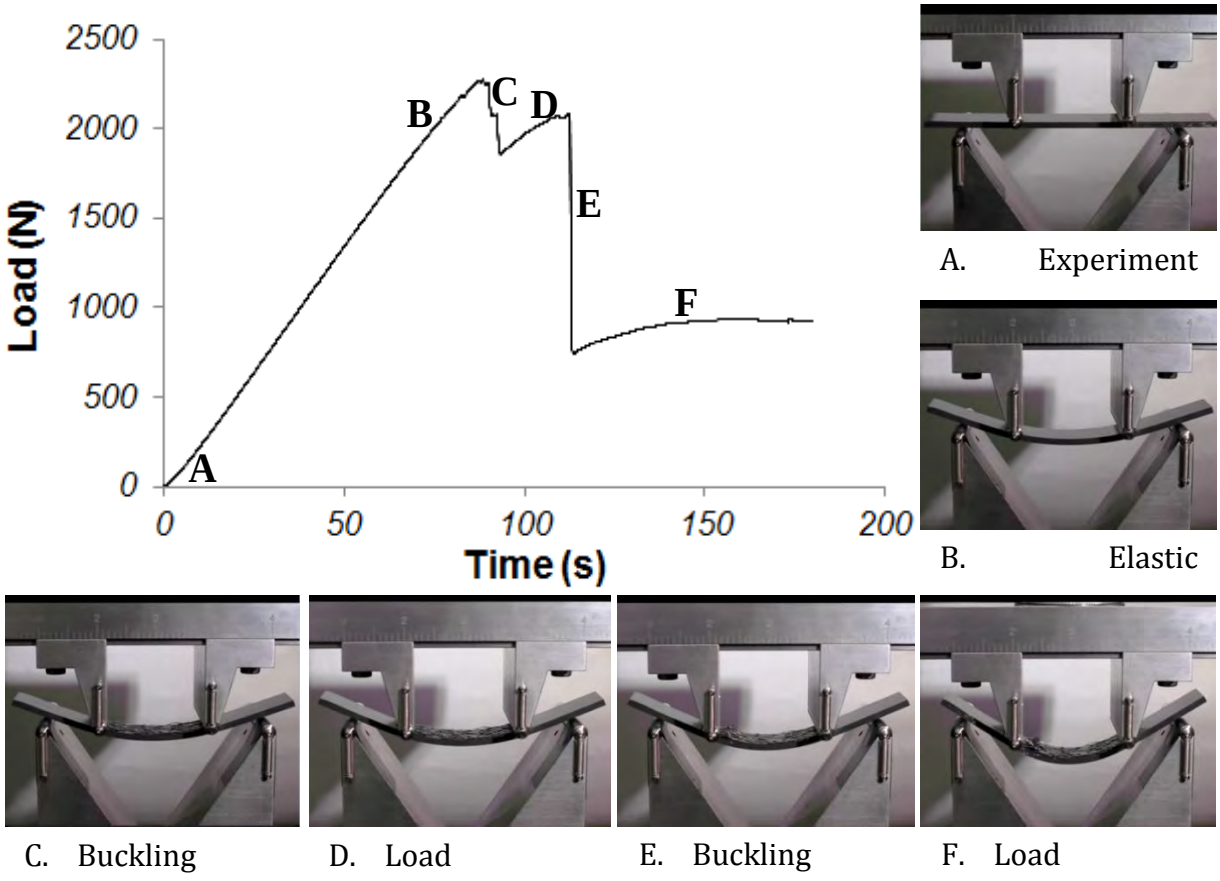

Figure 6: Typical flexural response with characteristic features identified

The flexural stress-strain and flexural modulus-strain results corresponding to the four tested flexural specimens can be seen superposed in Figure 7. As evident in this figure, the elastic response is relatively linear and results in a peak flexural modulus of approximately 66 GPa at a

strain of 0.8%. The instantaneous plot of the flexural modulus illustrates the initial softening behavior as the stress response increases at a decreasing rate. This continues until approximately 1.2% strain, at which point significant load drops are detected and 'failure' is defined. Physically, this failure has been identified as local buckling on a specimen's compressive side due to the warp fiber tows debonding from the ply. The subsequent sequence of events are illustrated in Figure 6, however the quantification of stress, strain, and modulus definitions are meaningless beyond the point of initial softening and failure.

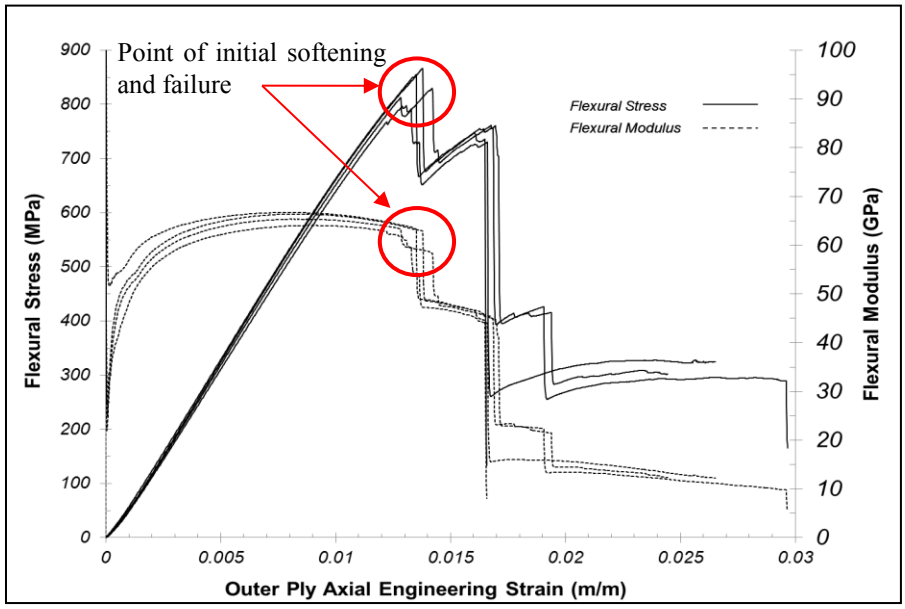

Figure 7: Summary of experimental results

4.1.2. Low-velocity Impact

Specimens were impacted at an incident kinetic energy of approximately 50 J. A second set of impact experiments with 25 J of incident kinetic energy were conducted to validate the model after necessary adjustments. Both measured force time histories are shown in Figure 8. The impact event consisted of a combination of elastic deformation and rebound as well as energy absorbing damage, with the entire event occurring in approximately 5 ms. Of the original 50 J of impact energy, approximately 23 J was absorbed into various forms of damage in the specimen while 27 J remained in the form of rebound velocity of the drop weight mass. A rebound brake was used in order to eliminate any subsequent impacts after the initial impact. This was important in order to correlate the damage observed post-mortem with the measured response. Average parameters for the lot of samples investigated are shown in Table 7.

Table 7: Average impact parameters measured during 50J experiments

	Impact Velocity	Impact Energy	Maximum Load	Energy Absorbed	Impact Duration	Rebound Velocity
Averages	*4.3 m/s*	*49.1 J*	*13575.1 N*	*22.9 J*	*5.0 ms*	*3.1 m/s*
Std Dev	*(0.002 m/s)*	*(0.047 J)*	*(317.8 N)*	*(0.953 J)*	*(0.069 ms)*	*(0.058 m/s)*

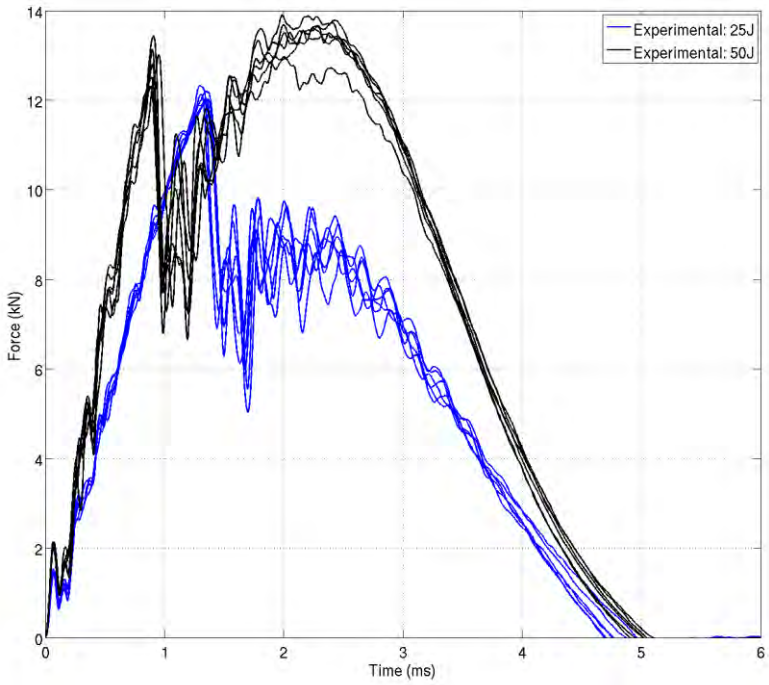

Figure 8: Force versus time from experiments

Typical impact response curves showing force, displacement and energy can be seen in Figure 9. The force is directly measured using a strain gage based load cell and, as previously mentioned, the velocity and displacements are determined with subsequent integration schemes using appropriate initial conditions. The data is filtered at 12 kHz in order to eliminate high frequency noise. The rebound velocity is not determined from the subsequent integration as errors have been observed due the filtering of data. Therefore, the rebound energy is calculated from the mass of the system and the rebound velocity, both of which are directly measured. This rebound energy is then subtracted from the incident impact energy to determine the total energy absorbed into the specimen. We assume all energy goes into either elastic deformation or damage. No consideration is given to thermal, acoustics, etc.

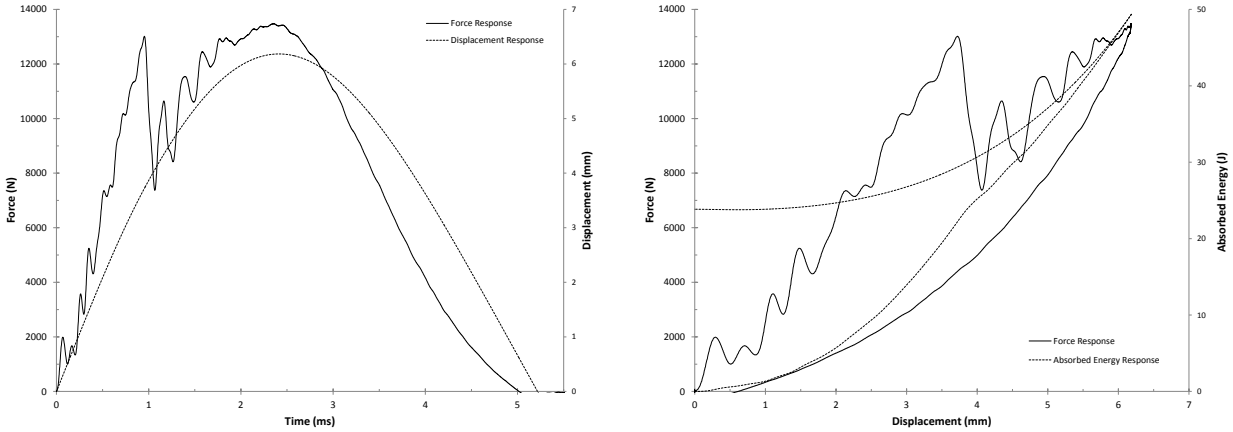

Force and Displacement – Time Response Force and Energy – Displacement Response

Figure 9: Typical response characteristics during the low-velocity impact event

Significant damage in the specimens occurs at approximately 3.7 mm of transverse displacement. This is noted by the approximate 43 % load drop that occurs, at which time the energy absorption shows a slight knee behavior. The absorbed energy during the event is continually increasing, primarily at an increasing rate up to the extent of the incident kinetic energy level. The rebound process then returns elastic potential energy in the form of kinetic energy by accelerating the drop weight mass back upwards. This is shown as the absorbed energy decreases as the crosshead returns to zero displacement.

The specimens underwent pre and post-impact scans using ultrasonics and 3D computed tomography. A typical series of pre and post scans can be seen in Figure 10. The amplitude of the back face reflection is plotted in these images and a corresponding scale is shown to quantify the degree of attenuation. A color coding with a large value of percent amplitude (AMP%) can be attributed to undamaged and well coupled material, allowing the input sound wave to pass through the specimen and return back to the transducer with virtually no losses. Conversely, low values of returned signal amplitude are attributed to attenuation of the signal in regions where damage is present, i.e. delamination, cracking, etc.

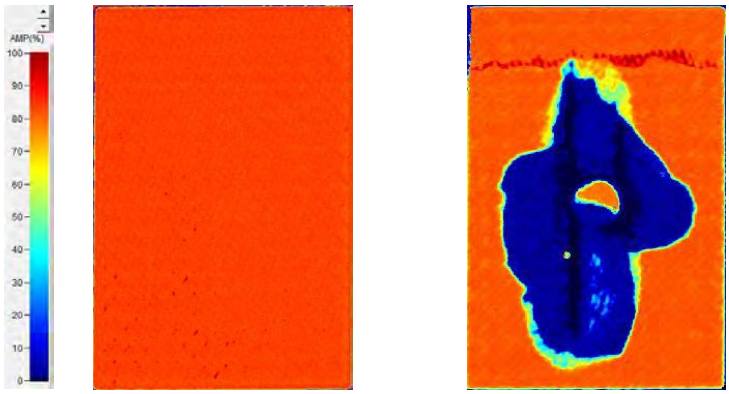

Ultrasonic Image Pre-scan *Ultrasonic Image Post-scan*

Figure 10: Typical pre and post-impact scans using ultrasonics

3D computed tomography is extremely insightful into the spatial distribution of damage and the extent of its growth. The form of damage can also be delineated in many instances with careful inspection after reconstruction. This provides an extremely useful tool for the validation of finite element simulations. As can be seen in Figure 11, the top-down view slices through the specimen reveal the extent of shear cracking and gross delamination. This top-down view is not able to detect delaminations that are in contact as well as the ultrasonic scans. However, as can be seen in Figure 12, slices along the length of the specimen reveal at which interfaces delamination has occurred and the extent at which it has grown. With image reconstruction software, a careful step-through of the specimen is conducted to map specific fracture and delamination fronts.

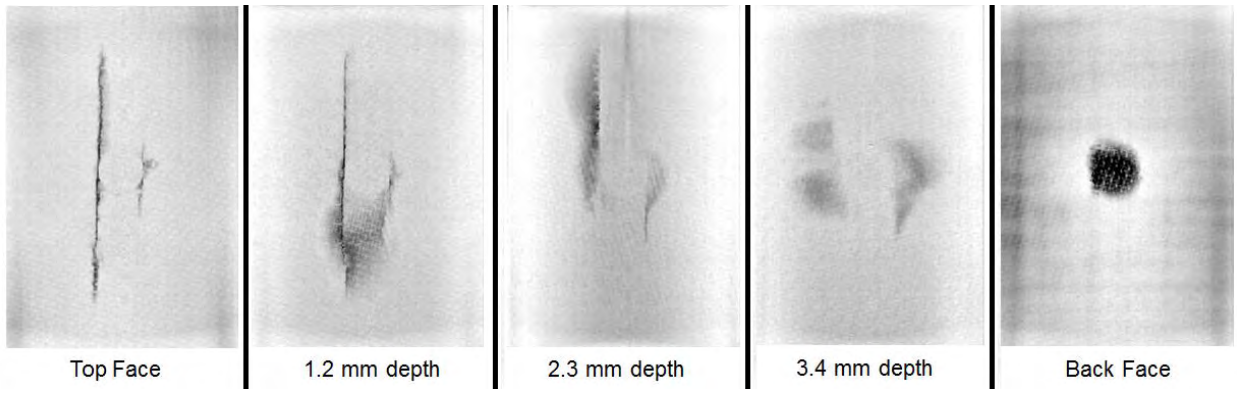

Figure 11: Typical reconstruction depth slices after impact using 3D CT

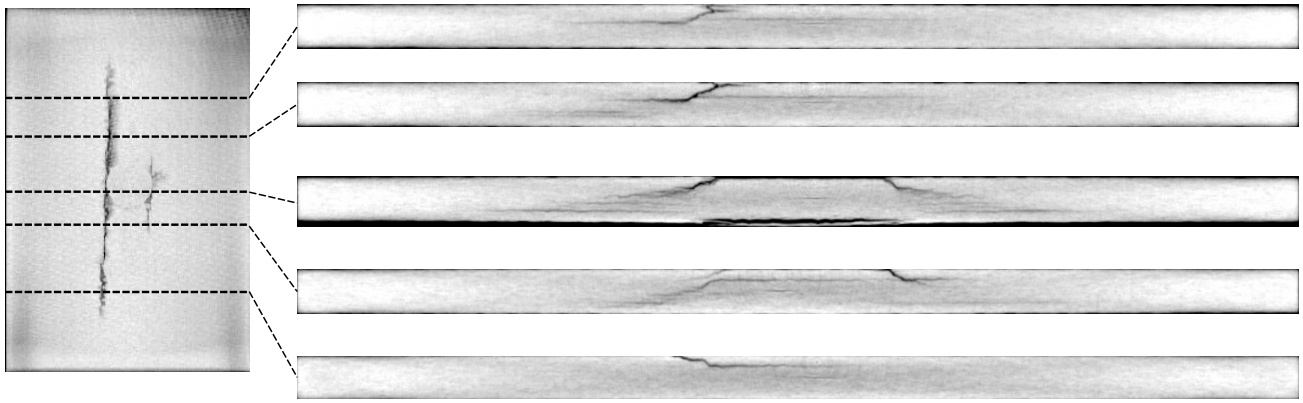

Figure 12: Typical CT slices along the specimen length showing respective cross sections

4.2. Validation and Uncertainty Quantification

4.2.1. Four-point Bend

Upon completion of a sensitivity analysis, some of the original *k* input parameters are specified as influential to the simulated response. Then, significant effort can be expended in the process of characterizing these critical input parameters exactly. However, it is possible that certain critical material parameters cannot be determined experimentally, possibly due to cost

constraints or lack in experimental expertise. For example, lacking suitable test fixtures, the out-of-plane compressive and shear properties for a fiber-reinforced, polymer composite material are difficult to determine experimentally. Nonetheless, it is likely that through additional numerical analyses or thorough literature surveys, accurate ranges in which the critical parameters may fall can be determined. Then, given uniform or normal distributions that describe the influential input parameters, uncertainty quantification can be used to propagate input parameter uncertainties though a simulation to determine the corresponding uncertainty in the predicted output response. This is readily achieved by sampling each input parameter range *n* times, creating *n* sets of sampled parameters. Then, *n* simulations can be processed in which the material model is defined with the *n* parameter sets. The resulting distribution of *n* simulation responses will represent the output range corresponding to the input parameter uncertainties [20].

The statistical method used to create the *n* parameter sets sampled from the input ranges is important as full coverage of the parameter space needs to be guaranteed. A sampling method that is commonly used to construct computer experiments is the Latin Hypercube Sampling (LHS) approach. Given a predefined number of sample points, *n*, the LHS method can be used to ensure that a random ensemble of sampled variables is truly representative of the parameter space. This is achieved through a simple two-step process. First, the variable ranges associated with each of the input parameters are divided into *n* "strata." Each of these strata is assigned an equal marginal sampling probability of 1/*n*. Next, the strata associated with each of the input parameters are individually sampled once and, when multiple parameters are sampled simultaneously, the inputs are randomly paired [21]. As this simple method ensures optimal coverage of the parameter space, it was chosen for the ensuing uncertainty quantification studies associated with this presented work.

The influencing material model parameters were defined within plausible ranges, uncertainty quantification was used to determine the corresponding ranges in the softening loads predicted for the tested flexural specimens. With the methods described in the previous section, the LHS method was used to sample the ranges of values specified in the above tables 100 times, creating 100 sets of sampled parameters. These parameter sets were then applied to the material models in 100 simulations performed with Sierra Adagio.

This process of creating and processing simulations was completed for four specimens, tested with the methods described in Section 2.2. For each specimen, upon completion of the computer experiments, the distribution created by the simulated responses was confirmed as normal with the adjusted Anderson-Darling test [22]. This test can be used to verify that a given sample comes from a population within a specific distribution, such as normal, and is described below in reference to the completed work. First, the adjusted Anderson-Darling statistic, A^{*2}, was determined from the 100 simulated responses corresponding to the four simulated specimens:

$$A^{*2} = (-N - S)\left(1 + \frac{0.75}{N} + \frac{2.25}{N}\right) \tag{31}$$

Where: N: number of simulated responses, 100

S: $$\frac{1}{N}\sum_{i=1}^{N}(2i-1)[\ln(F(Y_i)+\ln(1-F(Y_{N+1-i}))]$$

Y: the cumulative density function of the desired distribution ($F=\frac{1}{2}\left[1+\text{erf}\left(\frac{y-\mu}{\sigma\sqrt{2}}\right)\right]$ for a normal distribution)

Then, the statistic's value was compared to published data corresponding to the desired significance level to test for normality. Namely, for a normal distribution, a maximum adjusted Anderson-Darling statistic of 0.752 agrees with a significance level of 0.05.

With the aforementioned methods, the distributions of softening loads predicted for each of the four test specimens were verified as normal. Therefore, a histogram and normal distribution was fit to each set of 100 simulations and the mean value of the distribution was compared to the experimentally observed load at initial softening. Figure 13 shows a histogram and normal distribution representative of the uncertainty quantification process and Table 8 summarizes the simulation and experimentally observed data.

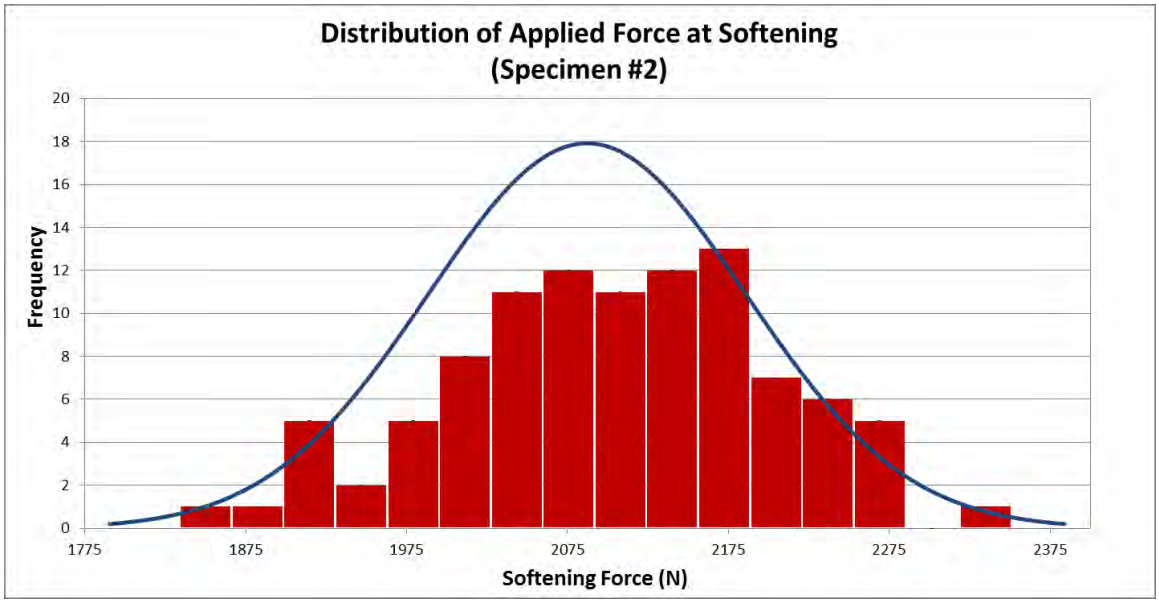

Figure 13: Representative distribution of uncertainty analysis simulation output

Table 8: Summary of experimental and simulation results

Specimen ID	Actual Softening Load (N)	Predicted Softening Load Means (N)	% Difference
1	*2185.8*	*2098.2*	*4.1*
2	*2181.9*	*2087.1*	*4.4*
3	*2237.6*	*2087.4*	*6.9*
4	*2243.4*	*2087.6*	*7.2*

As shown in Table 8, the difference in the mean values of the predicted softening loads is small with the largest deviation occurring with specimen 4. Based on the initial guesses for model inputs, the predicted softening loads were consistently lower than the experimentally observed values. Specifically, through the application of the two-sample t-statistic on the combined samples, there is only a 1.6% (p-value = 0.016) chance of a softening load prediction exceeding an experimentally observed value [23]. Furthermore, if the t-distribution is used to determine the precision interval associated with the distribution of predicted softening loads, it can be concluded with 95% certainty (α = 0.05), that the bounds in the difference (error bounds) between the model and experimental predictions for the softening load are [-319, 74.9] N or [-14.4, 3.39] % when compared to the experimental mean [24]. These conclusions may indicate that the actual properties of the carbon fiber composite material correspond better to the parameter sets used to define the simulations sorted into the higher histogram bins. However, the percent differences between the predicted responses and the experimentally observed behaviors are small. This indicates that uncertainty quantification can be used to make accurate predictions in the absence of exact material property values. Therefore, calibration of the parameters influential to the softening load, namely the compressive strength in the warp direction, is completed to match the softening loads. The result is a calibrated compressive strength associated with softening just prior to surface lamina bucking of F_{1C} = -816 MPa with a standard deviation of 69.0 MPa.

4.2.2. Low Velocity Impact

Validation and uncertainty quantification is used to assess the predictive capability of the model, i.e. how well can the model predict experimental behavior in tests that were not used for calibration. Qualitative (subjective) assessment of the damage and quantitate (objective) change in kinetic energy are used as validation metrics. Since the uncertainty distribution is unknown for many of the inputs, a uniform distribution is assumed in the sampling algorithm. LHS with 100 simulations is utilized to generate an ensemble of models to provide an output distribution.

A common method to determine if two normally distributed samples are of the same population is the Student's t-test. The t-test can be used to test whether there is sufficient evidence to assume the model sample means are equal to the real world estimates (experiments). The p-value associated with the t-test is the probability that, if the null hypothesis of equal means were true, the differences are obtained by chance. For example: a value of 0.05 means there is 0.05 probability of error when rejecting the null hypothesis. In terms of validation, a high probability results in accepting the null hypothesis that there is no significant difference between the model and the real world. Therefore, higher values of p (typically > 0.05) indicate more confidence in the model.

Applying the Anderson-Darling test [22], normality is confirmed with a test statistics of 0.294 for the energy absorbed and 0.418 for the rebound velocity. Utilizing the Levene test for equal variance [25], it is confirmed that the model and experimental variances can be treated as equal. Therefore, a t-test for unrelated groups with equal variance can be used to estimate model validity. Testing the hypothesis that the model and the experiment means of the energy absorbed are equal produces a p-value of 0.095 which is greater than the commonly used critical value

0.05. There is insufficient evidence to reject the null hypothesis. The t-statistic is then utilized to give a precision interval. The difference in the means is estimated by

$$\delta X \approx \left(\bar{X}_{model} - \bar{X}_{exper}\right) \pm t_{\alpha/2,df}\hat{\sigma}_{\bar{X}_{model}-\bar{X}_{exper}} \tag{32}$$

where combined standard deviation of the differences is

$$\hat{\sigma}_{\bar{X}_{model}-\bar{X}_{exper}} = S_{pooled}\sqrt{\frac{1}{n_{model}} + \frac{1}{n_{exper}}}$$

and the pooled standard deviation assuming equal variance is

$$S_{pooled} = \sqrt{\frac{(n_{exper}-1)S_{exper}^2 + (n_{model}-1)S_{model}^2}{n_{exper}+n_{model}-2}} \tag{33}$$

With 95% certainty ($\alpha = 0.05$), the bounds in the difference (error bounds) between the model and experimental predictions for means of energy absorbed are [-5.17, 2.43] or [-22.6, 10.6] %.

Since the impact velocity is a model input, the rebound velocity is also used as the validation metric. The t-test produces a p-value of 0.096 and the 95% error bounds are estimated as [-0.142, 0.299] m/s or [-4.548, 9.618] %. While the mean of the model response matches well to the experimental values, the deviation is high, reducing confidence in the model. This is likely a product of the uncertainty associated with choosing material parameters without adequate experimental backing. However, when utilizing this model for predictions, this error is a necessity when quantifying uncertainty on margins.

Next, a qualitative (subjective) assessment of the model outputs is done. The delaminated area and crack characteristics are assessed to determine accuracy in the model fidelity and physical representation of failure. Figure 14 provides an example selected at random of the out-of-plane shear damage accumulated in the model and a CT scan of a tested specimen. While the experiment shows a more resolved crack and a more distributed delamination pattern, the overall damaged area matches well with the model. The length and position of the main crack extending axially (into the page) matches experiments. Figure 15 gives a selection of experimental and model 2D delamination areas. A minor discrepancy exists in the extent of delamination. Nearly all the models predicted delamination to the shorter edge, while nearly all the experiments exhibited contained delamination. Similarly, the 2D analysis of delaminated area is greater in the models. However, the actual area of delamination was not explicitly measured. Overall, the qualitative properties matched well between model and experiment.

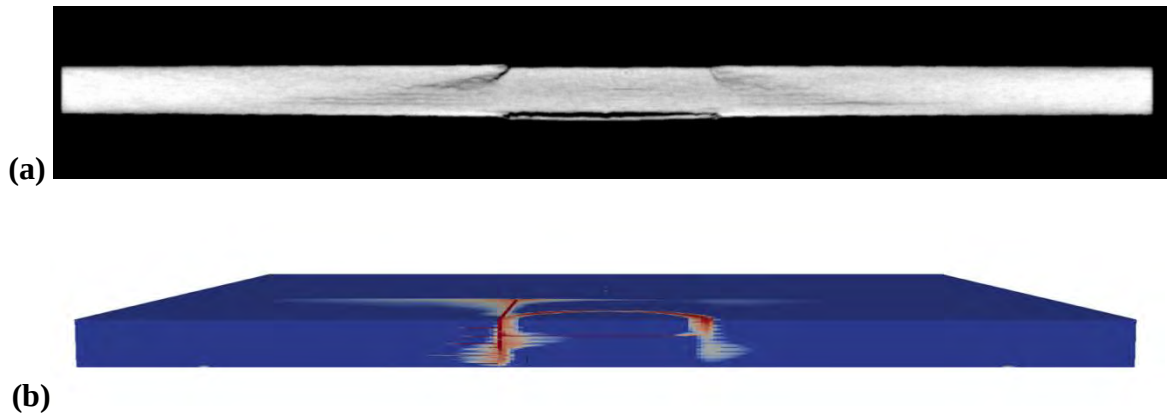

Figure 14: The post impact cross-section of (a) CT scanned specimen and (b) model prediction of weft damage and delamination. Note, the scan is taken from a material with slightly different matrix but otherwise identical

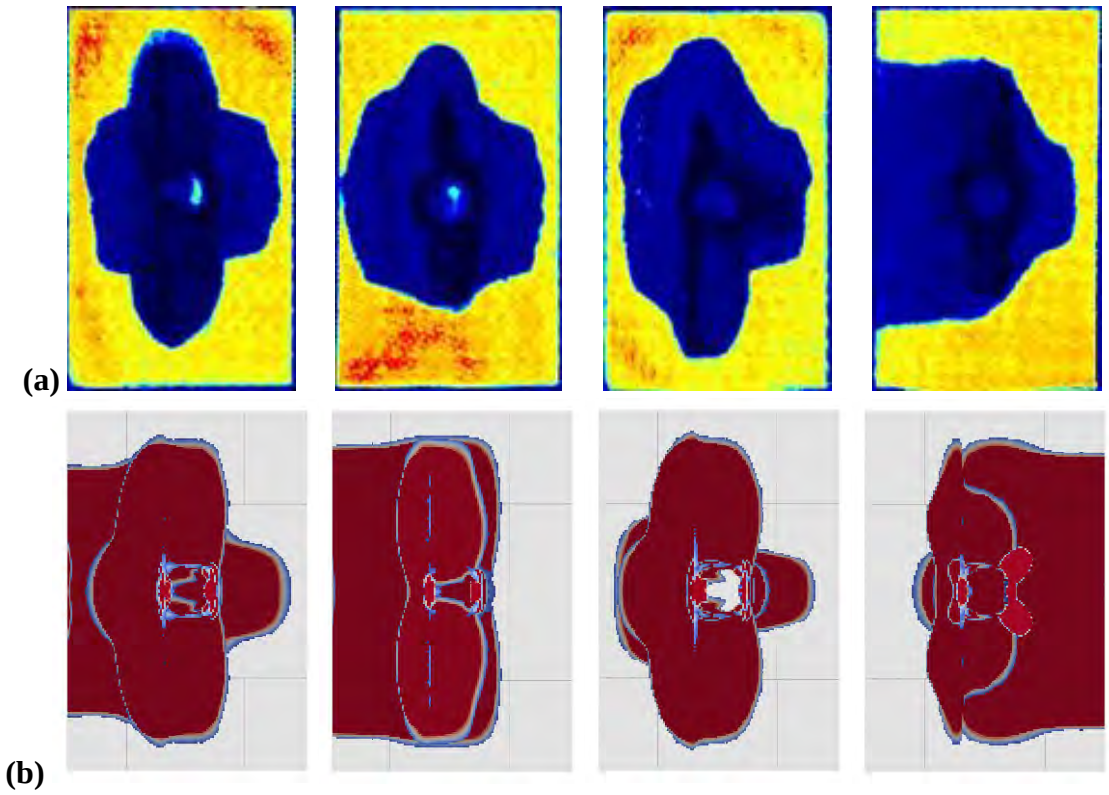

Figure 15: A selection of delaminated areas for (a) experiments and (b) simulations

Figure 16 gives force versus time for all the simulations and experiments. While both the homogenized quantitative metrics and qualitative aspects of the model match well with experiments, there are many important discrepancies to note. Firstly, the rate of damage evolution, time over which the drops due to damage occur, is lower for the experiments as seen in the larger peak and sudden drop off from elastic loading. Noting these discrepancies and

evaluating the sensitivity analysis results, the estimated parameters of importance can be calibrated to produce a response that is qualitatively and quantitatively similar to the experiments.

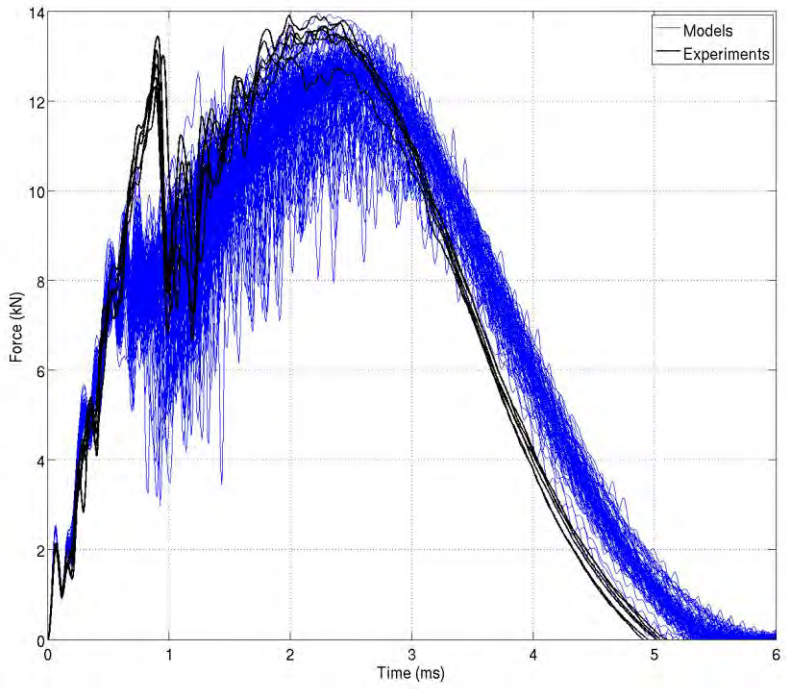

Figure 16: Force versus time from simulations and experiments

4.3. Calibration and Further Experiments

4.3.1. Calibration to the 50J experiments

Based on this effort, the model form errors are isolated with ease. The most noteworthy discrepancy is in the load time histories. Through data analysis and calibration, the sharp peak at first failure is a result of delamination immediately subsequent to crack initiation with delamination incurring the greatest energy loss. This is consistent with the model, which predicted delamination and crack growth to occur in much the same way yet more gradually and at a lower load. The higher loads in the experiments must be associated with a higher effective strength. The sensitivity analysis indicated the interlaminar shear properties to be the most influential on the force associated with first failure. However, it proved impossible to calibrate the interlaminar properties with this force because with increasing interlaminar strength, the out of plane fracture properties became more influential. It was necessary to decrease the out-of-plane shear fracture energy with increasing interlaminar toughness in order to provide both qualitative and quantitative accuracy. The reduced resistance to shear crack growth distributed delamination to at least two layers, thus increasing the load required for initiation.

In order to address these hypotheses, a simulation is implemented with a higher mode II interlaminar toughness ($G_{II}^{*} = 1.5G_{II}$) and related peak stress ($\tau_{max}^{*} = 1.5\tau_{max}$) and an out-of-plane shear fracture toughness reduction ($G_{II23}^{*} = 0.4G_{II23}$). The results are shown in Figure 17. This simple change provides a better estimate for the sudden load drop seen in the experiments. Similar to the filtering in the experimental data, a slight smoothing is done to the model data to remove high frequency noise.

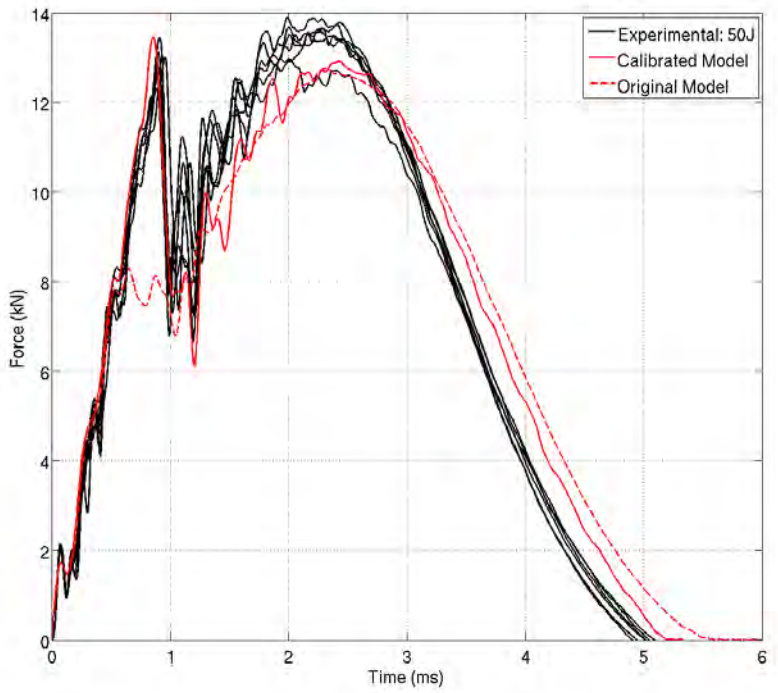

Figure 17: An example of a calibrated simulated force versus time

Interestingly, the calibrated model produced a bimodal distribution when sampled with LHS (n = 99, one simulation failed to finish). The entire dataset does not produce valid results as the low energy peak is well outside the experimental data (see Figure 18). However, utilizing only the top 50% of the results (values > median), the simulations match very well to the experiments. Confirming both normality and equal variance for this data set as before, the t-test produces a p-value of 0.44 and a bound on the differences of [-3.2, 1.4] J or [-13.9, 6.1]%.

Figure 19 shows the force versus time for all the calibrated simulations. As expected, the first peak better matches the experiments. On average the first peak is better captured in the high energy mode. Conversely, the second peak appears to be predicted better in the low energy mode. Additionally, the high energy absorption mode has more oscillations.

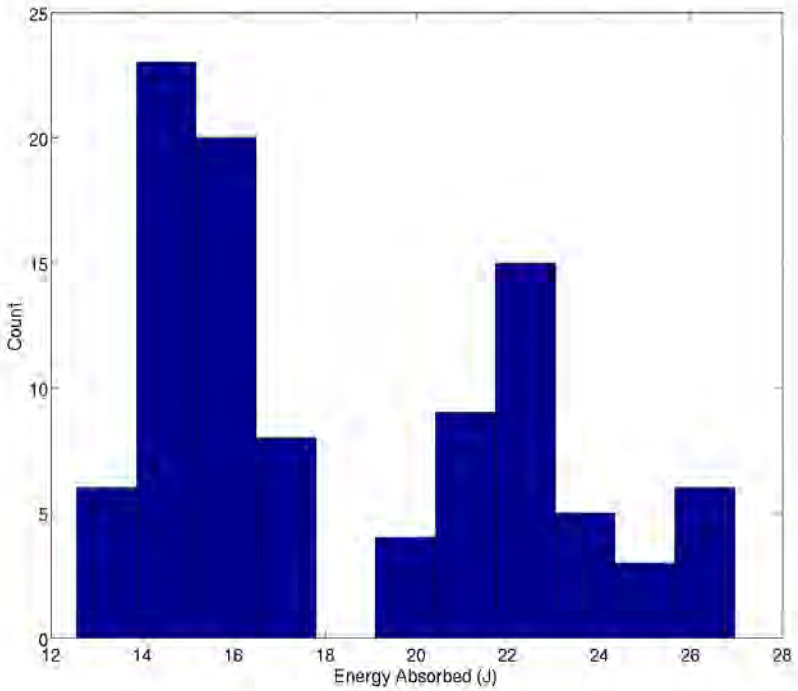

Figure 18: Histogram showing energy absorbed for calibrated simulations

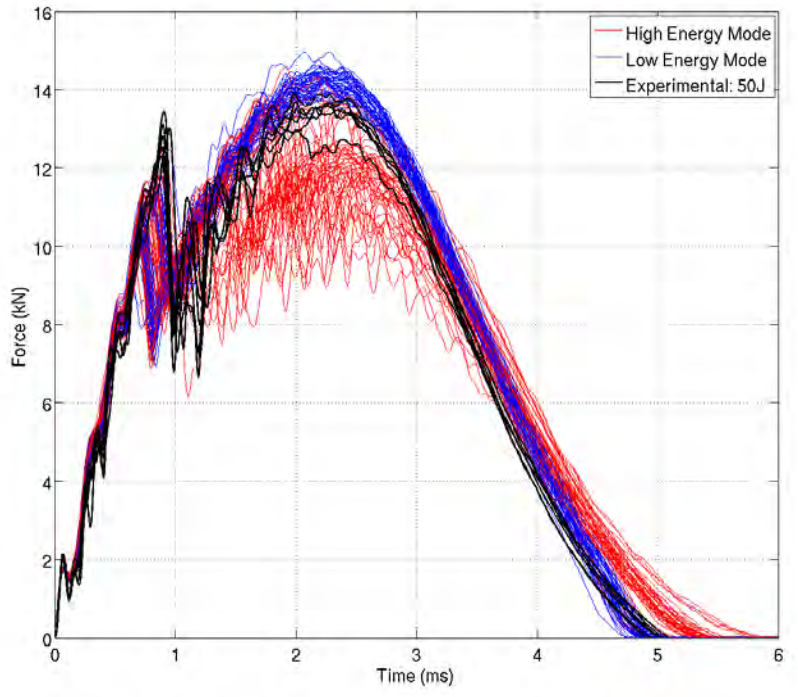

Figure 19: Force versus time from 50J calibrated simulations with experiments

While many qualitative similarities exist between the simulations with low and high energy absorptions, two notable differences exist. Firstly, most simulations with delaminations to the edge are found in the high energy distribution and most with contained delaminations are found in the low energy distribution. Secondly, the most likely the cause of bimodality is the difference in the number of major delaminations. There are two distinct delamination planes in the most of the simulations with high energy absorption mode and only one major delamination in the low energy mode. Figure 20 shows four delaminations from simulations selected randomly from groups of equal size, each with increasing energy absorption.

Investigating the differences in the input parameters normalized by the individual means between both distributions, illuminates the complexity of the problem. The t-test is again utilized to investigate the difference between parameter groups. Input parameter sets with large values of the t-test statistic are significantly different between groups. Three parameters, the mode II interlaminar toughness and peak stress and the out-of-plane compressive strength, are considered significant (p-value > 0.05). To elaborate, the high energy absorption mode utilizes higher values of compressive strength and lower values of interlaminar toughness and peak stress compared to the low energy absorption mode. Assuming the addition of further replicate experiments would produce a unimodal response with the majority of samples exhibiting two or more planes of delamination, these parameters point to deficiencies in the model.

It is clear the balance between out-of-plane lamina failure and delamination is the most significant process affecting energy absorption. One plane versus two planes of delamination appears to be a function of the depth of the first delamination which always nucleates with lamina failure and is consistent across the distribution. The depth of the first delamination appears to directly correlate with the depth of the crack (number of failed plies). If a shallow delamination occurs, a second is more likely due to the increased shear in the thicker laminate. Therefore, the appearance of a second delamination is associated with high lamina strength and low interlaminar toughness. Since with lower interlaminar toughnesses the qualitative results do not agree, the following deficiencies are postulated. Firstly, the cohesive material formulation cannot account for rate dependencies due to the viscoelastic effect. Significant energy dissipation without delamination and increased strength associated with the viscoelastic effect is postulated. Therefore, viscoelasticity in the interlaminar response and potentially in the bulk response may be required to obtain better results. Secondly, the significance of the out-of-plane compressive strength points to inaccuracies in the coupling behavior of the bulk material model. The material model likely inaccurately couples the shear and normal components of strain in predicting failure.

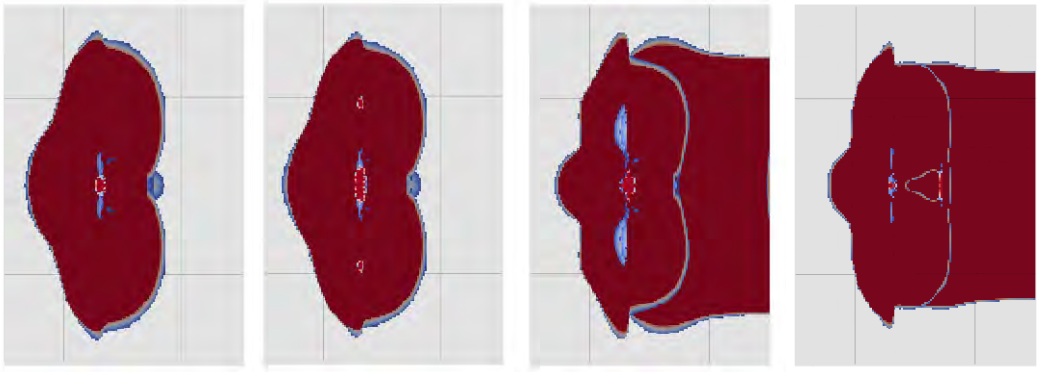

Figure 20: A selection of 50J calibrated delaminated selected randomly from each quartile of energy absorption increasing left to right

4.3.2. Validation with 25J

While calibration indicated a need for higher mode II interlaminar fracture toughness, this is a measured parameter. While it is possible that the measured value is in error; the more likely explanation is inaccurate physics. Therefore, both scenarios are tested. First, a model only with lower out-of-plane shear fracture energies is simulated. Second, the calibration factors described above are added. To test the predictive capability with these two parameter sets, an impact energy was chosen to be significantly different than the previous value while still activating similar phenomenon. The 50 J experiments showed recoverable loading (matching elastic predictions) up to approximately 25 J of energy transfer. Therefore, we chose and impact energy of 25 J for subsequent experiments. The experimental results are shown in Table 9.

Table 9: Average impact parameters measured during 25 J experiments

	Impact Velocity	Impact Energy	Maximum Load	Energy Absorbed	Impact Duration	Rebound Velocity
Averages	*3.06 m/s*	*25.4 J*	*12120 N*	*11.1 J*	*4.76 ms*	*2.30 m/s*
Std Dev	*(0.0008 m/s)*	*(0.012 J)*	*(132 N)*	*(0.64 J)*	*(0.11 ms)*	*(0.057 m/s)*

A total of 200 and 100 samples are simulated with LHS for the decreased out-of-plane shear toughness model and fully calibrated model respectively.

The decreased out-of-plane shear toughness simulation results are as follows. Applying the Anderson-Darling test, normality cannot be confirmed within reasonable confidence. The test statistics for energy absorbed and rebound velocity are 5.89 and 6.69 respectively. A histogram of energy absorption shows positive skew (skewness = 1.22), i.e. a high energy tail, (Figure 23). This is likely due to the choice of energy input close to energy required for failure. Therefore, previously applied t-test is not applicable and the skewness must be taken into account.

The Mann-Whitney [26] non-parametric rank test is utilized for the energy absorbed and rebound velocity. Testing the null hypothesis of equal median ranks between the model and experiment produces p-values of 0.007 and 0.008 for energy absorbed and rebound velocity respectively.

This p-value gives justification to reject the null-hypothesis in favor of the alternative hypothesis that the ranks are different. This test will likely be more conservative than the previously employed t-test. Nevertheless, quantified validation is not achieved. Figure 21 shows the force versus time for both model and experiment. As expected the load at first failure is under predicted.

Similar quantitative results are obtained from the calibrated model. The energy data is positively skewed (skew = 1.28). Therefore, the Mann-Whitney non-parametric rank test p-values for energy absorbed and rebound velocity are 0.000 and 0.000, respectively; indicating no justification for model validation. However, the force time results for the calibrated model, shown in Figure 22, match very well. Therefore, maximum force is utilized in the calibrated simulations in order to quantify force time differences. While not skewed, normality is not confirmed for the maximum force in the model. Therefore, the non-parametric rank test p-value for the difference in model and experiment peak forces is calculated as 0.04. While still below the commonly used value of 0.05, this metric yields much higher confidence.

Qualitatively, the results are similar to the 50 J simulations. The qualitative metrics such as crack length and depth (not shown) and delaminated area, (Figure 24a, b and c), match well. While not shown here due to space considerations, nearly every low toughness model delaminates to a free edge similar to the 50 J simulations and, as with the experiments, all the calibrated models have contained delaminations. Nevertheless, there is no quantitative justification for model validation at this energy level. Similar to the 50 J study, the models under predict energy absorption. The magnitude of under prediction appears similar. Consequently the relative difference is higher, resulting in little justification for quantifiable validation. Since with better qualitative results, the quantitative results suffer and quantitative validation is confirmed with higher energy impacts, there must be physical inaccuracies in the model. Therefore, it is suggested that the results of the 25 J validation effort further substantiate inaccuracies in the cohesive zone formulation. While the fracture energies associated with delamination are consistent with experiments, the load to delamination is under predicted in low-velocity impact conditions.

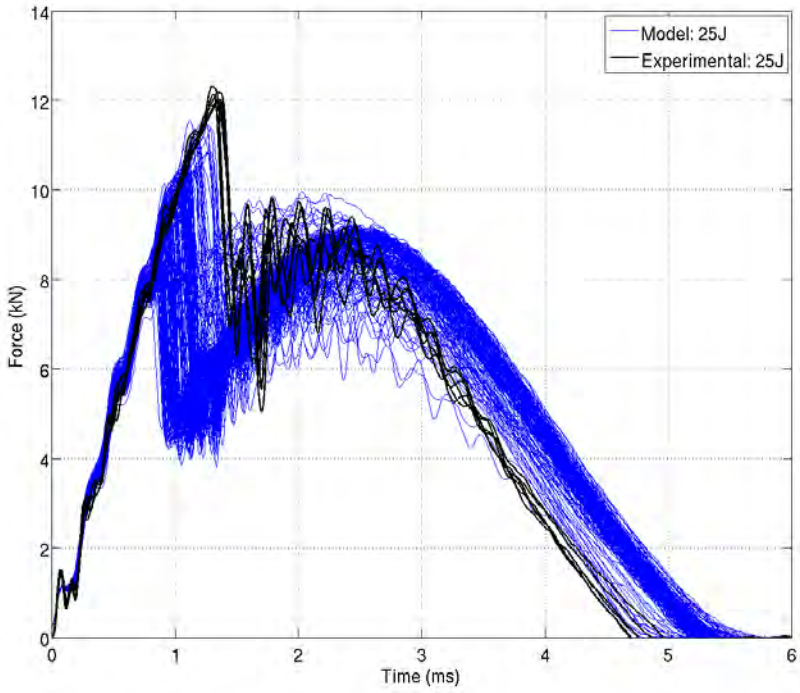

Figure 21: Force versus time from 25J decreased out-of-plane shear toughness simulations with experiments

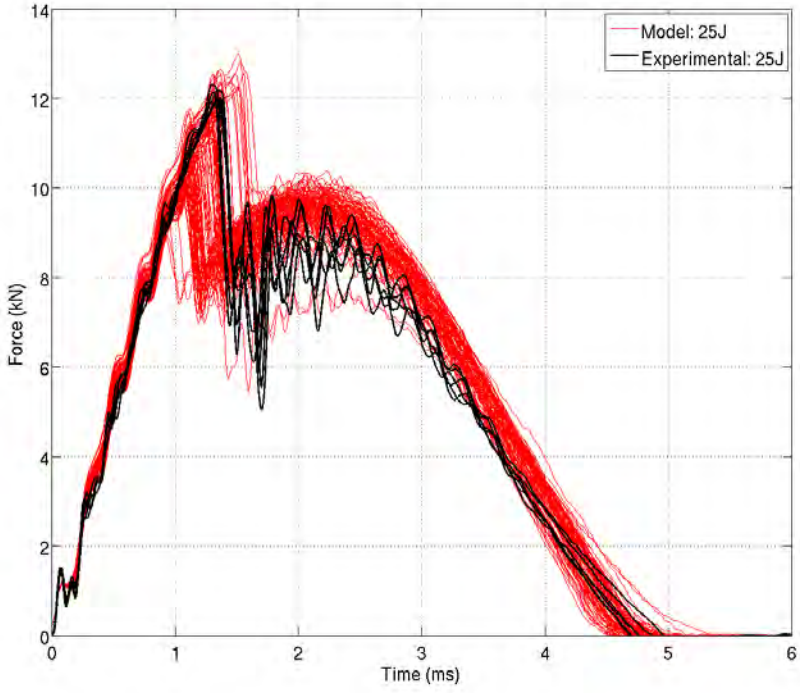

Figure 22: Force versus time from 25J calibrated simulations with experiments

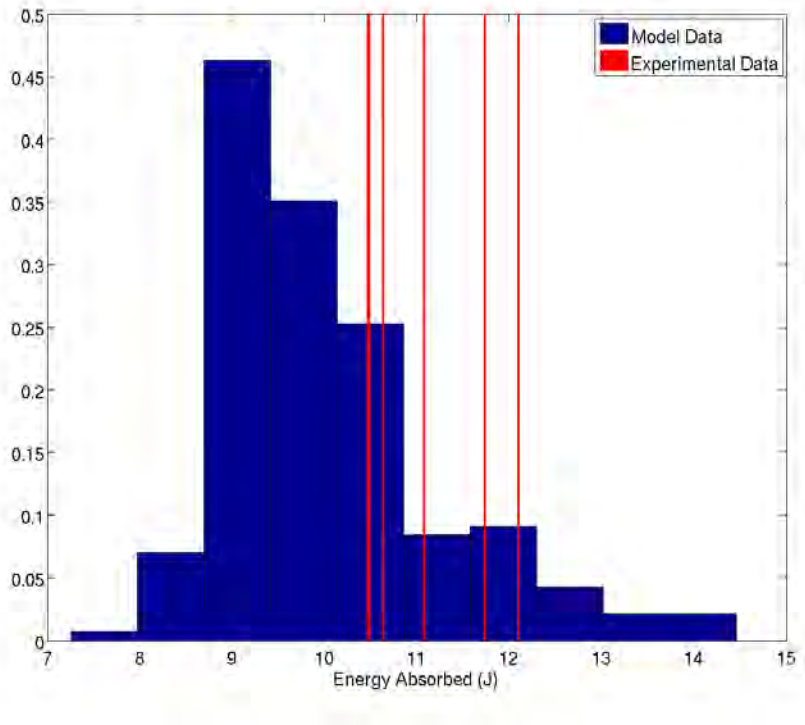

Figure 23: Normalized histogram of energy absorbed from the 25J simulations with experimental data shown as vertical lines

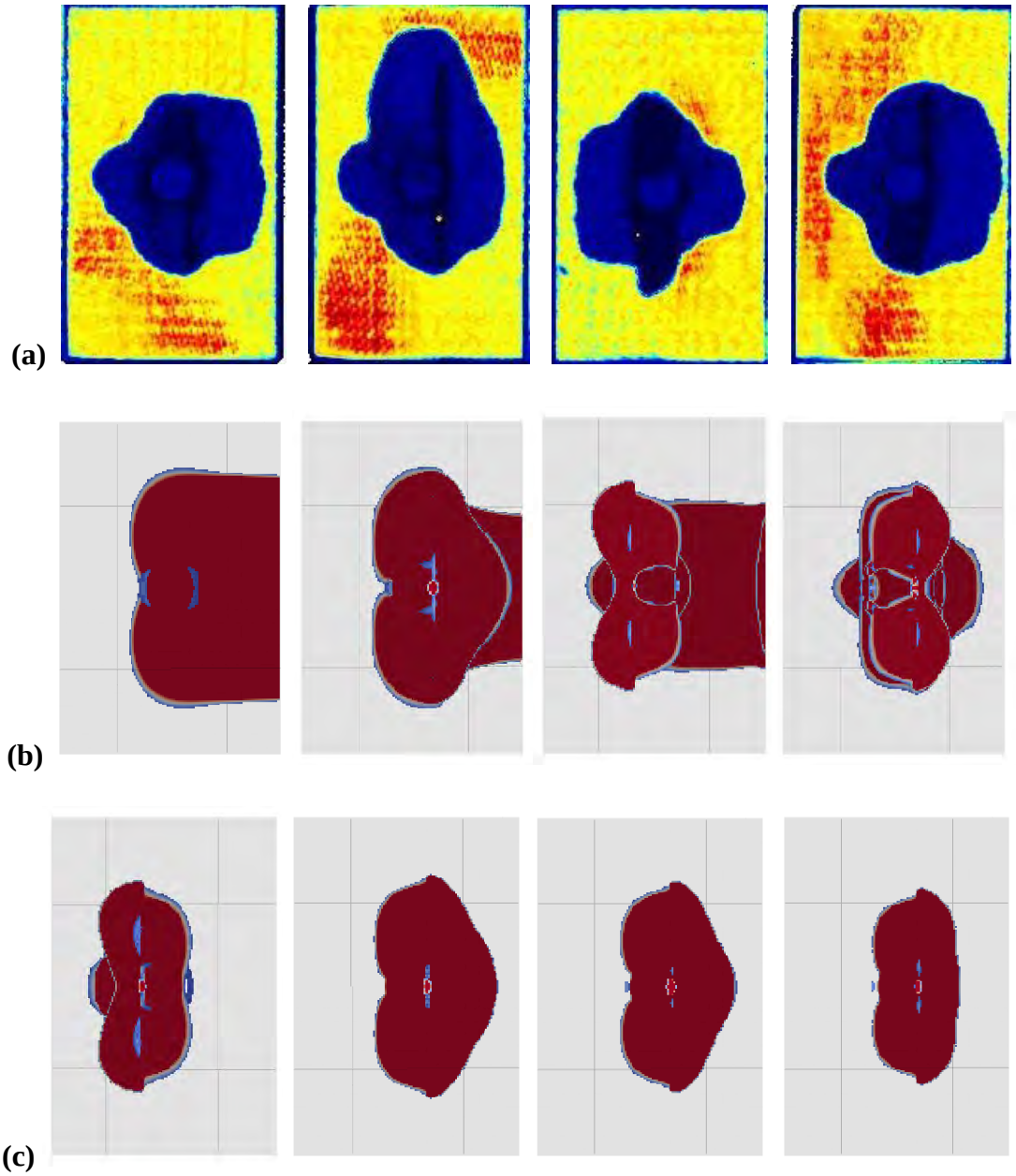

Figure 24: A selection of 25J delaminated areas for (a) experiments, (b) low energy model and (c) calibrated model

5. CONCLUSIONS

The results of this study have demonstrated a thorough verification and validation effort for the simulation of composite damage and failure under low-velocity impact. A simulation methodology and model formulation is presented with good results. Further experimentation and model development is nonetheless necessary.

For a 50J impact experiment, statistical justification in favor of the equal distribution hypothesis between the model and experiment is achieved and the uncertainty bounds are calculated. The qualitative simulation results compared well with experiments. The model predicted matrix damage, fiber breaks and delaminations consistent with experiments. However, the simulations tended to over predict the extents of delamination. Nearly all the models predicted the delaminated areas reaching the short edge of the specimen. This phenomenon was only observed in a few experimental specimens. Similar results are found in the 25J impacts. The qualitative results matched very well. However, the data was positively skewed and therefore under predicted the energies. Utilizing statistical methods for non-normal data could not give objective justification for model validation at this level.

Based on this effort, the model form errors are isolated with. The most noteworthy discrepancy is in the load time histories. Through data analysis and calibration, the sharp peak at first failure is a result of delamination immediately subsequent to crack initiation with delamination incurring the greatest energy loss. This is consistent with the model, which predicted delamination and crack growth to occur in much the same way yet more gradually and at a lower load. The higher loads in the experiments must be associated with a higher effective strength. It is postulated that the primary deficiencies are lack of material data for the complex conditions experienced in the experiment, namely combined compression and shear, and failure model form error for the interactive formulation utilized in the lamina calculations and the delamination predictions in the cohesive elements. At this point it is certain that better characterization data is necessary, however, constitutive model modification, particularly cohesive zone materials, is not ruled out.

ACKNOWLEDGEMENTS

Many experimentalists and NDE specialists supported this work. Specimen preparation and mechanical testing was completed by Roger Watson (8252), Timothy Gilbertson (8223) and Robert Oteri (8223). Ultrasonic imaging and computed tomography was completed by Karen Krafcik (8223), David Moore (1522) and Burke Kernen (1522). The low-velocity impact testing and post processing was funded through WSEAT. Additionally, Patricia Hough provided help with the statistics.

REFERENCES

[1] "Guide for Verification and Validation in Computational Solid Mechanics," ASME, Ed., ed. New York, NY: American Society of Mechanical Engineers, 2006.

[2] L. Bryson and A. Salehian, "Sensitivity Analysis of Selected Input Parameters for an Advanced Constitutive Model," *Geotech Geol. Eng.,* vol. 32, pp. 247-258, 2014.

[3] R. Gunawan, M. Jung, R. Braatz, and E. Seebauer, "Parameter Sensitivity Analysis Applied to Modeling Transient Enhance Diffusion and Activation or Boron in Silicon," *J. of the Electrochemical Soc.,* vol. 150, pp. 758-765, 2003.

[4] S. Hua, Z. Zhu, and L. Zhang, "Vehicle Body Structural Parameter Optimization Based on Dynamics Simulation," in *International Conference on Advanced Technology Design and Manufacture*, Valencia, Spain, 2010.

[5] J. Huang, C. Krousgrill, and A. Bajaj, "Modeling of Automotive Drum Brakes for Squeal and Parameter Sensitivity Analysis," *J. of Sound and Vibration,* vol. 289, pp. 246-263, 2006.

[6] I. Kenis, J. Urai, and M. Sintubin, "The Development of Bone-Shaped Structures Initially Segmented Layers During Layer-Parallel Extension: Numerical Modeling and Parameter Sensitivity Analysis," *J. of Struct. Geo.,* vol. 28, pp. 1183-1192, 2006.

[7] H. Zheng, X. Yu, J. Hu, and Q. Yan, "Parameter Sensitivity Analysis of Vertical Deflection for Long-Span Continuous Rigid-frame Bridge," *Adv. Mat. Research,* vol. 163-167, pp. 1500-1504, 2011.

[8] S. English, A. Brown, and T. Briggs, "A Micro to Macro Approach to Polymer Matrix Composites Damage Modeling: Final LDRD Report," Sandia National Laboratories, Livermore, CA2013.

[9] E. J. Barbero, P. Lonetti, and K. K. Sikkil, "Finite element continuum damage modeling of plain weave reinforced composites," *Comp. Part B,* vol. 37, pp. 137–147, 2006.

[10] F. S., R. Bruns, H. Ferreira, G. Matos, J. David, G. Brandao*, et al.*, "Box-Behnken Design: An Alternative for the Optimization of Analytical Methods," *Analytica Chimica ACTA,* vol. 597, pp. 179-186, 2007.

[11] C. Croarkin and P. Tobias. Engineering Statistics Handbook [Online].

[12] A. Matzenmiller, J. Lubliner, and R. Taylor, "A constitutive model for anisotropic damage in fiber-composites," *Mech. of Mat.,* vol. 20, pp. 125-152, (1995).

[13] P. Maimí, P. Camanho, J. Mayugo, and C. Dávila, "A continuum damage model for composite laminates: Part I – Constitutive model," *Mech. of Mat.,* vol. 39, pp. 897-908, (2007).

[14] P. Maimí, P. Camanho, J. Mayugo, and C. Dávila, "A continuum damage model for composite laminates: Part II – Computational implementation and validation," *Mech. of Mat.,* vol. 39, pp. 909-919, (2007).
[15] Z. P. Bazant and B. H. Oh, "Crack band theory for fracture of concrete," *Matériaux et Construction,* vol. 16, pp. 155-177, 1983.
[16] *User's Manual for LS-Dyna MAT162 Unidirectional and Plain Weave Composite Progressive Failure Models*. Newark, DE: Center for Comp. Mat., 2011.
[17] S. Li, M. Thouless, A. Waas, J. Schroeder, and P. Zavattieri, "Mixed-mode Cohesive-zone Models for Fracture of an Adhesively-bonded Polymer-matrix Composite," *Eng. Fract. Mech.,* vol. 73, pp. 64-78, (2006).
[18] K. W. Gan, S. R. Hallett, and M. R. Wisnom, "Measurement and modelling of interlaminar shear strength enhancement under moderate through-thickness compression," *Comp. Part A,* vol. 49, pp. 18-25, (2013).
[19] I. Daniel, B. Werner, and J. Fenner, "Strain-rate-dependent failure criteria for composites," *Comp. Sci. and Tech.,* vol. 71, pp. 357-364, 2011.
[20] W. Niccoli, F. Marinelli, T. Fairbanks, and R. Dancause, "Latin Hypercube Sampling: Application to Pit Lake Hydrologic Modeling Study," in *Conf. on Hazardous Waste Research*, Montreal, Canada, 1998.
[21] M. McKay, R. Beckman, and W. Conover, "A Comparison of Three Methods for Selecting Values of Input Variables in the Analysis of Output From a Computer Code," *Technometrics,* vol. 42, pp. 55-61, 2000.
[22] R. D'Augostino and M. Stephen, *Goodness-of-fit Techniques*. New York, NY: Marcel Dekker, 1986.
[23] D. Moore, *The Basic Practice of Statistics*. New York, NY: W. H. Freeman and Company, 2010.
[24] R. Figliola and D. Beasley, *Theory and Design for Mechanical Measurements*. New York, NY: John Wiley and Sons, 2000.
[25] H. Levene, "Robust testes for equality of variances," in *Contributions to Probability and Statistics*, I. Olkin, Ed., ed Palo Alto, CA: Stanford Univ. Press, 1960, pp. 278–292.
[26] H. B. Mann and D. R. Whitney, "On a Test of Whether one of Two Random Variables is Stochastically Larger than the Other," *Annals of Math. Stat.,* vol. 18, pp. 50-60, 1947.
[27] W. Oberkampf and C. Roy, *Verification and Validation in Scientific Computing*. Cambridge, UK: Cambridge University Press, 2010.
[28] R. G. Hills, W. R. Witkowski, W. J. Rider, T. G. Trucano, and A. Urbina, "Development of a Fourth Generation Predictive Capability Maturity Model," Sandia National Laboratories, Albuquerque, NM2013.
[29] Sierra Product Owners, "Sierra Support for PCMM," Sandia National Laboratories, Albuquerque, NM, Internal MemoMarch 27, 2013 2013.

APPENDIX A: PHENOMENA IDENTIFICATION RANKING TABLE

The Phenomena Identification Ranking Table (PIRT) is used to rank all important physical phenomena and assess the initial and final state of the mathematical model, code implementation and validation. The PIRT uses high (H), medium (M) and low (L) designations for the ranking. The table is then color coded to indicate potential consequences if errors are present. Adequate representations are shown in green. Inadequacies are shown in yellow and red for one and two deviations respectively. While a PIRT is typically done at the beginning and end of the validation processes, in this work this process is only completed at the end. However, for some physical phenomena such as delamination and composite fracture, the results of this study could provide justification for higher rankings in these categories. Table A-1 provides the ranking for all important physics after validation efforts.

Table A-1: PIRT for low velocity impact simulations

Phenomena	Importance	Math Model	Sierra/SM Code	Validation
Contact	*H*	*H*	*M*	*M*
Delamination	*H*	*M*	*M*	*M*
Orthotropic Elasticity	*H*	*H*	*M*	*M*
Composites Failure	*H*	*M*	*M*	*L*
Friction Between Delaminated Faces	*M*	*H*	*M*	*L*
Material Rate Dependence	*M*	*L*	*L*	*L*
Enforcement of Boundary Conditions	*H*	*H*	*H*	*L*
Inertial Loads	*H*	*H*	*H*	*M*

For this particular application the adequacy of the model is clearly in question; particularly in the areas of contact, delamination and fracture. The issues with adequacy can and will be addressed with a suit of single physics tests and the development of sophisticated model modifications. Nevertheless, the validation results of this study have justified considerable confidence in the model.

APPENDIX B: PCMM ASSESSMENT

The predictive capability maturity model (PCMM) assessment is completed on the low-velocity impact of carbon fiber fabric reinforced polymer simulations in Sierra explicit dynamics finite element code. The PCMM is used to assess the completeness of the modeling activity [27]. Refer to the PCMM template version 1.3 and SAND report [28] for detailed definition of each element. The final results of the assessment are shown as radar plots in Figure B-2. It should be noted that much of this work is published in peer reviewed conference papers. However, this level of review is not taken into consideration for this assessment. The individual element target rational and achievement justification are presented as follows:

CVER Desired Levels:

The Code Verification (CVER) element assesses the quality control aspects of the software employed. For this study, apart from post processing tools and various scripts, the software used is the Sierra explicit dynamics code Presto. Thus, CVER1, 3 and 4 of the this element are completed in a memo produced by the Sierra software team [29]. The desired level of CVER2 was chosen to be 2 based on the need for one and two-way coverage tests as well as the verification that the most up to date version (Master) is tested. However, it is not expected the tests will cover all the features required for the application. The desired level of CVER5 was chosen to be 1 based on the plan for an internal review of the verification activities.

CVER Achieved Levels:

The CVER2 sub-element is given a ranking of 2 because the feature coverage tool is utilized to document one and two-way feature testing as well as verifications. Figure B-1 give a visual of the two way coverage. Code verification activities are reviewed by group members justifying CVER5 rank or 1.

Table B-1: Code verification PCMM element

Code Verification (CVER)		Desired	Achieved
CVER1	Apply Software Quality Engineering (SQE) processes	2	2
CVER2	Provide test coverage information	2	2
CVER3	Identification of code or algorithm attributes, deficiencies and errors	2	0
CVER4	Verify compliance to Software Quality Engineering (SQE) processes	2	2
CVER5	Technical review of code verification activities	1	1

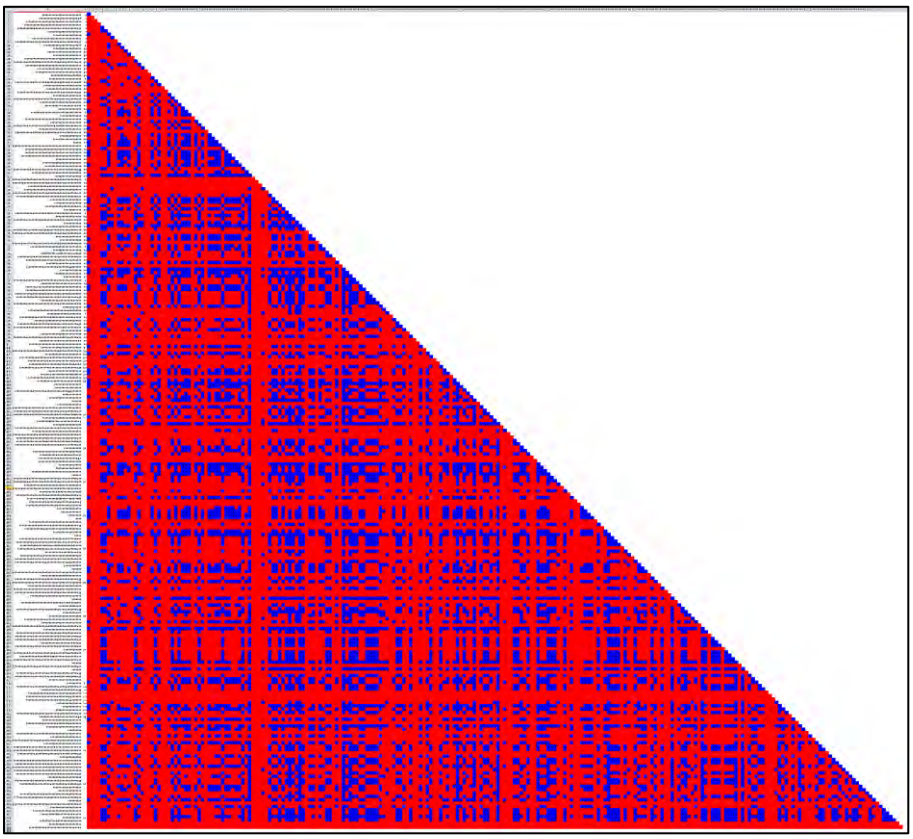

Figure B-1: FCT two-way coverage visual

PMMF Desired Levels:

The Physics and Material Model Fidelity (PMMF) element assesses the validation and application space of models used in the analysis. The desired level of PMMF1 was chosen to be 2 because while some physics are assumed negligible, most are correlated with the PIRT. The desired level for PMMF2 was 2. Many important experiments used for material characterization will be validated with simulations compared to experimental data. Since this study is a research validation effort, the PMMF3 element was given a desired level of 3 because the application and the validation domains are the same. The validation plan for this study includes peer review and a companion document on the material model. Therefore, the PMMF4 sub-element is given a desired level of 2.

PMMF Achieved Levels:

The PMMF1 sub-element is given a ranking of 2. The PIRT for this analysis is completed and documented in Appendix A. To the extent that experimental data exists, separate effects model validation and evaluation of experimental uncertainty is done, justifying a rank of 2 for the PMMF2 sub-element. As stated above, the PMMF3 element is given a level of 3 because the application and the

validation domains are the same. While the majority of this work is presented in a peer reviewed conference proceeding, much of the review for the material models is completed by the analysis team. Therefore, the PMMF4 sub-element is given a ranking of 1.5.

Table B-2: Physics and Material Model Fidelity PCMM element

Physics and Material Model Fidelity (PMMF)		Desired	Achieved
PMMF1	Characterize completeness versus the PIRT	2	2
PMMF2	Quantify model accuracy (i.e., separate effects model validation)	2	2
PMMF3	Assess interpolation vs. extrapolation of physics and material model	3	3
PMMF4	Technical review of physics and material models	2	1.5

RGF Desired Levels:

The Representation and Geometric Fidelity (RGF) element assesses the geometric fidelity and verification. It is expected that much of the experimental apparatus can be ignored, however, most of the actual components in the load path will be given high fidelity. Therefore, the RGF1 sub-element was given a desired level of 2. The RGF2 sub-element was given a desired level of 2 because the geometric sensitivity of some major components will be discussed and quantified. The experimentalist will review but not certify the geometric representation, giving a desired level of 2 for sub-element RGF3.

RGF Achieved Levels:

The RGF1 sub-element is given a ranking of 2. The RGF2 sub-element is given a ranking of 1.5. Of the three major assumptions made in the geometric representation only one is addressed with simulations. The experimentalist reviewed but did not certify the geometric representation, giving a level of 2 for sub-element RGF3.

Table B-3: Representation and Geometric Fidelity PCMM element

Representation and Geometric Fidelity (RGF)		Desired	Achieved
RGF1	Characterize Representation and Geometric Fidelity	2	2
RGF2	Geometry sensitivity	2	1.5
RGF3	Technical review of representation and geometric fidelity	2	2

SVER Desired Levels:

The Solution Verification (SVER) element assesses the how well the errors in the numerical solution are addressed. The desired ranking for SVER1 was level 2, because the errors will be estimated and reported through various mesh convergence studies but not included in the response. The quantification of the uncertainty should be evaluated, giving a target of level 2 for SVER2. The input deck for simulations will be inspected by an external analyst, thus a desired level of 2 is given to SVER3. All post processing scripts will be evaluated by the V&V team, giving a desired level of 2 for SVER 4. An external review of the verification efforts should be included in this effort; therefore the desired level of SVER5 is 2.

SVER Achieved Levels:

The SVER1 sub-element is given a ranking of 1.5. While numerical errors were estimated, error bars where not implemented. Moreover, the numerical solution parameters where optimized but the sensitivity of the model was not addressed. The uncertainty in computational error was not addressed; therefore SVER2 is given a score of 0. As planned, the input deck was inspected by an external analyst, justifying a level 2 for sub-element SVER3. The post-processing scripts where only verified by the analyst, justifying a level of 1 for SVER4. Without consideration of publications, the solution verification efforts are only verified by the project team members giving a justification of level 1 for SVER5.

Table B-4: Solution Verification PCMM element

Solution Verification (SVER)		Desired	Achieved
SVER1	Quantify numerical solution errors	2	1.5
SVER2	Quantify Uncertainty in Computational (or Numerical) Error	2	0
SVER3	Verify simulation input decks	2	2
SVER4	Verify simulation post-processor inputs decks	2	1
SVER5	Technical review of solution verification	2	1

VAL Desired Levels:

The Validation Hierarchy (VAL) element assesses the validation methodology and application effort. For this is a coupon level validation, the presented hierarchy has one level that will be completed. The desired levels for VAL1 and VAL2 are ones. While much of the validation will be qualitative, objective justification will only be completed on quantitative results. Thus, a desired level

of 2 is given to sub-element VAL3. No assertions are to be given on the application domain, therefore the VAL4 sub-elements has little relevance. Nevertheless, since in this case the application domain is arbitrary, a level of 3 is desired for VAL4. An external review of the validation efforts should be included in this effort; therefore the desired level of VAL5 is 2.

VAL Achieved Levels:

The VAL1 and VAL2 sub-elements both assigned a 1 since only the coupon level validation is addressed in the validation hierarchy. While qualitative validation is included, this study provides quantitative validation on quantities of interest. This justifies a score of 2 for VAL3. The application domain should be inferred at the level of validation supporting a score of 3 for VAL4. Without consideration of publications, the validation efforts are only verified by the project team members giving a justification of level 1 for VAL5.

Table B-5: Validation PCMM element

Validation (VAL)		Desired	Achieved
VAL1	Define a validation hierarchy	1	2
VAL2	Apply a validation hierarchy	1	2
VAL3	Quantify physical accuracy	2	2
VAL4	Validation domain vs. application domain	3	3
VAL5	Technical review of validation	2	1

UQ Desired Levels:

The Uncertainty Quantification (UQ) element assesses how the various model uncertainties are addressed. Most of the uncertainties will be identified and characterized as aleatoric or epistemic. However, no separation is deemed necessary. Thus, a desired level of 1 is given to UQ1. All the uncertainties identified in UQ1 will be included in a sensitivity analysis. Nevertheless, some uncertainties will not be included in either. Therefore, UQ2 is given a desired level of 2. As noted above aleatoric and epistemic will be included as continuously distributed variables. Therefore, UQ3 should be at level 1. Since the validation hierarchy has only one stated level, the roll-up is trivial. Nevertheless, a level of 2 is given to UQ4, since most major uncertainties are included. An external review of the uncertainty quantification efforts should be included in this effort; therefore the desired level of UQ5 is 2.

UQ Achieved Levels:

The UQ1 sub-element is given a ranking of 1. The simulations included both epistemic and aleatoric uncertainties rolled up in a single sampling. A thorough sensitivity analysis was performed, however some uncertainties are not included, for example the tup shaft stiffness is assumed. Therefore, a level of 2 is achieved for UQ2. A level of 1 is achieved for UQ3. The impact of aleatoric and epistemic uncertainties are reported but not separated. Aggregation or roll-up is performed for most of the major uncertainties, justifying a level 2 for UQ4. Without consideration of publications, the uncertainty quantification portion of this study is only verified by the project team members giving a justification of level 1 for UQ5.

Table B-6: Uncertainty Quantification PCMM element

Uncertainty Quantification (UQ)		Desired	Achieved
UQ1	Aleatoric and epistemic uncertainties identified and characterized.	1	1
UQ2	Perform sensitivity analysis	2	2
UQ3	Quantify impact of uncertainties from UQ1 on quantities of interest	1	1
UQ4	UQ aggregation and roll-up	2	2
UQ5	Technical review of uncertainty quantification	2	1

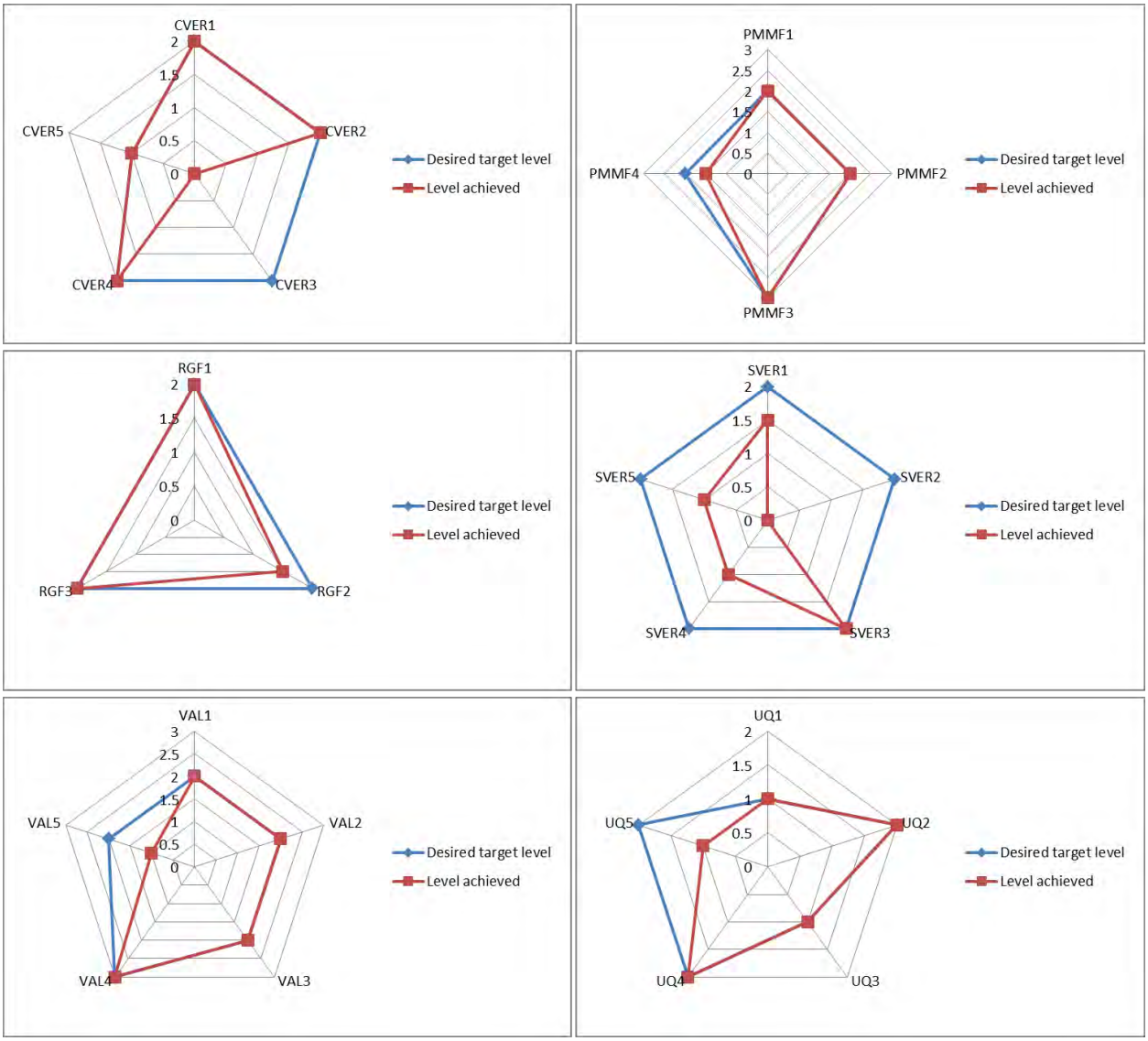

Figure B-2: LVI PCMM radar plots

APPENDIX C: ANOVA RESULTS

Table C-1: Four-point bend deflection point

Source	Sum Sq.	d.f.	Mean Sq.	F	Prob>F
E11	1.40E+05	2	6.98E+04	1.36E+03	0.000
E22	2.16E-01	2	1.08E-01	2.12E-03	0.998
E33	1.52E+03	2	7.62E+02	1.49E+01	0.000
NU12	1.59E+04	2	7.93E+03	1.55E+02	0.000
NU23	1.61E+01	2	8.06E+00	1.58E-01	0.854
NU13	7.03E+02	2	3.51E+02	6.86E+00	0.001
G12	2.33E+03	2	1.17E+03	2.28E+01	0.000
G23	6.30E+01	2	3.15E+01	6.16E-01	0.540
G13	1.27E+03	2	6.36E+02	1.24E+01	0.000
TENSILE_FIBER_STRENGTH_11	3.43E+00	2	1.72E+00	3.36E-02	0.967
COMPRESSIVE_FIBER_STRENGTH_11	8.54E+02	2	4.27E+02	8.34E+00	0.000
TENSILE_FIBER_STRENGTH_22	2.05E+01	2	1.03E+01	2.01E-01	0.818
COMPRESSIVE_FIBER_STRENGTH_22	1.80E+01	2	9.02E+00	1.76E-01	0.839
TENSILE_MATRIX_STRENGTH_33	1.60E+00	2	8.02E-01	1.57E-02	0.985
COMPRESSIVE_MATRIX_STRENGTH_33	2.26E+03	2	1.13E+03	2.21E+01	0.000
TENSILE_FIBER_STRENGTH_33	1.91E+02	2	9.57E+01	1.87E+00	0.154
COMPRESSIVE_FIBER_STRENGTH_33	1.41E+01	2	7.04E+00	1.38E-01	0.872
SHEAR_MATRIX_STRENGTH_12	6.25E+00	2	3.12E+00	6.11E-02	0.941
SHEAR_FIBER_STRENGTH_12	6.32E+01	2	3.16E+01	6.18E-01	0.539
SHEAR_MATRIX_STRENGTH_23	3.98E+01	2	1.99E+01	3.89E-01	0.678
SHEAR_FIBER_STRENGTH_23	1.43E+01	2	7.14E+00	1.39E-01	0.870
SHEAR_MATRIX_STRENGTH_13	7.95E+02	2	3.97E+02	7.77E+00	0.000
SHEAR_FIBER_STRENGTH_13	2.54E+03	2	1.27E+03	2.48E+01	0.000
TENSILE_FRACTURE_ENERGY_11	9.23E+00	2	4.62E+00	9.02E-02	0.914
COMPRESSIVE_FRACTURE_ENERGY_11	4.84E+01	2	2.42E+01	4.73E-01	0.623
TENSILE_FRACTURE_ENERGY_22	3.98E+01	2	1.99E+01	3.89E-01	0.678
COMPRESSIVE_FRACTURE_ENERGY_22	2.46E+00	2	1.23E+00	2.41E-02	0.976
TENSILE_FRACTURE_ENERGY_33	1.35E+01	2	6.76E+00	1.32E-01	0.876
COMPRESSIVE_FRACTURE_ENERGY_33	9.20E+00	2	4.60E+00	8.99E-02	0.914
SHEAR_FRACTURE_ENERGY_12	1.67E+01	2	8.34E+00	1.63E-01	0.850
SHEAR_FRACTURE_ENERGY_23	1.57E-01	2	7.85E-02	1.54E-03	0.999
SHEAR_FRACTURE_ENERGY_13	3.33E+00	2	1.67E+00	3.26E-02	0.968
MAXIMUM_COMPRESSIVE_DAMAGE_11	1.78E+01	2	8.88E+00	1.74E-01	0.841
MAXIMUM_COMPRESSIVE_DAMAGE_22	3.67E-02	2	1.83E-02	3.58E-04	1.000
MAXIMUM_COMPRESSIVE_DAMAGE_33	1.43E+00	2	7.12E-01	1.39E-02	0.986
COMPRESSION_COUPLING_FACTOR_11	3.67E-02	2	1.83E-02	3.58E-04	1.000
COMPRESSION_COUPLING_FACTOR_22	3.67E-02	2	1.83E-02	3.58E-04	1.000
COMPRESSION_COUPLING_FACTOR_33	3.67E-02	2	1.83E-02	3.58E-04	1.000
TENSILE_DAMAGE_MODULUS_33	1.79E+00	2	8.97E-01	1.75E-02	0.983
COMPRESSIVE_DAMAGE_MODULUS_33	1.86E+02	2	9.30E+01	1.82E+00	0.163
SHEAR_DAMAGE_MODULUS_12	4.15E+00	2	2.08E+00	4.06E-02	0.960
SHEAR_DAMAGE_MODULUS_23	2.30E+01	2	1.15E+01	2.25E-01	0.799
SHEAR_DAMAGE_MODULUS_13	3.91E+03	2	1.96E+03	3.82E+01	0.000
HARDENING_EXPONENT_33	1.83E+02	2	9.14E+01	1.79E+00	0.168
HARDENING_EXPONENT_12	1.87E+00	2	9.37E-01	1.83E-02	0.982
HARDENING_EXPONENT_23	2.18E+00	2	1.09E+00	2.13E-02	0.979
HARDENING_EXPONENT_13	3.22E+03	2	1.61E+03	3.15E+01	0.000
Error	2.17E+05	4230	5.12E+01		
Total	4.38E+05	4324			

Table C-2: LVI energy absorbed

Source	Sum Sq.	d.f.	Mean Sq.	F	Prob>F
E11	4.36E-01	2	2.18E-01	3.50E+01	0.000
E22	7.03E-01	2	3.52E-01	5.65E+01	0.000
E33	1.10E-02	2	5.52E-03	8.87E-01	0.412
NU12	2.05E+00	2	1.03E+00	1.65E+02	0.000
NU23	1.64E+00	2	8.22E-01	1.32E+02	0.000
NU13	5.93E-03	2	2.96E-03	4.77E-01	0.621
G13	1.16E+00	2	5.80E-01	9.33E+01	0.000
G23	1.22E-03	2	6.11E-04	9.83E-02	0.906
G12	9.64E-02	2	4.82E-02	7.75E+00	0.000
TENSILE_FIBER_STRENGTH_11	2.12E-04	2	1.06E-04	1.70E-02	0.983
TENSILE_FIBER_STRENGTH_22	4.58E-01	2	2.29E-01	3.68E+01	0.000
TENSILE_FIBER_STRENGTH_33	3.31E-03	2	1.65E-03	2.66E-01	0.767
TENSILE_MATRIX_STRENGTH_33	1.78E-01	2	8.88E-02	1.43E+01	0.000
COMPRESSIVE_FIBER_STRENGTH_11	5.86E-02	2	2.93E-02	4.72E+00	0.009
COMPRESSIVE_FIBER_STRENGTH_22	3.51E-01	2	1.75E-01	2.82E+01	0.000
COMPRESSIVE_FIBER_STRENGTH_33	1.89E+01	2	9.47E+00	1.52E+03	0.000
COMPRESSIVE_MATRIX_STRENGTH_33	1.13E+01	2	5.67E+00	9.11E+02	0.000
SHEAR_FIBER_STRENGTH_12	2.80E-04	2	1.40E-04	2.25E-02	0.978
SHEAR_FIBER_STRENGTH_23	1.28E-03	2	6.41E-04	1.03E-01	0.902
SHEAR_FIBER_STRENGTH_13	2.87E-04	2	1.44E-04	2.31E-02	0.977
SHEAR_MATRIX_STRENGTH_12	4.06E+00	2	2.03E+00	3.27E+02	0.000
SHEAR_MATRIX_STRENGTH_23	4.31E-01	2	2.15E-01	3.47E+01	0.000
SHEAR_MATRIX_STRENGTH_13	1.02E-01	2	5.10E-02	8.20E+00	0.000
TENSILE_FRACTURE_ENERGY_11	1.94E-04	2	9.71E-05	1.56E-02	0.985
TENSILE_FRACTURE_ENERGY_22	2.08E+03	2	1.04E+03	1.68E+05	0.000
TENSILE_FRACTURE_ENERGY_33	1.30E-04	2	6.49E-05	1.04E-02	0.990
COMPRESSIVE_FRACTURE_ENERGY_11	7.32E-02	2	3.66E-02	5.89E+00	0.003
COMPRESSIVE_FRACTURE_ENERGY_22	1.66E-02	2	8.31E-03	1.34E+00	0.263
COMPRESSIVE_FRACTURE_ENERGY_33	6.22E-03	2	3.11E-03	5.00E-01	0.607
SHEAR_FRACTURE_ENERGY_12	4.55E-04	2	2.28E-04	3.66E-02	0.964
SHEAR_FRACTURE_ENERGY_23	1.35E-03	2	6.74E-04	1.08E-01	0.897
SHEAR_FRACTURE_ENERGY_13	1.15E-04	2	5.74E-05	9.23E-03	0.991
TENSILE_DAMAGE_MODULUS_33	8.56E-03	2	4.28E-03	6.89E-01	0.502
COMPRESSIVE_DAMAGE_MODULUS_33	4.20E+00	2	2.10E+00	3.38E+02	0.000
SHEAR_DAMAGE_MODULUS_12	1.38E-03	2	6.89E-04	1.11E-01	0.895
SHEAR_DAMAGE_MODULUS_13	2.02E-01	2	1.01E-01	1.62E+01	0.000
SHEAR_DAMAGE_MODULUS_23	2.45E-03	2	1.23E-03	1.97E-01	0.821
HARDENING_EXPONENT_12	1.17E-02	2	5.85E-03	9.41E-01	0.390
HARDENING_EXPONENT_23	2.87E-04	2	1.43E-04	2.31E-02	0.977
HARDENING_EXPONENT_13	1.01E-02	2	5.05E-03	8.12E-01	0.444
HARDENING_EXPONENT_33	3.57E+00	2	1.78E+00	2.87E+02	0.000
MAXIMUM_COMPRESSIVE_DAMAGE_11	1.93E-03	2	9.65E-04	1.55E-01	0.856
MAXIMUM_COMPRESSIVE_DAMAGE_22	2.10E-04	2	1.05E-04	1.68E-02	0.983
MAXIMUM_COMPRESSIVE_DAMAGE_33	1.35E-01	2	6.73E-02	1.08E+01	0.000
COMPRESSION_COUPLING_FACTOR_11	1.82E-04	2	9.09E-05	1.46E-02	0.986
COMPRESSION_COUPLING_FACTOR_22	1.18E-04	2	5.92E-05	9.52E-03	0.991
COMPRESSION_COUPLING_FACTOR_33	2.35E-04	2	1.17E-04	1.89E-02	0.981
CZ_ENERGY_I	2.67E-01	2	1.33E-01	2.14E+01	0.000
CZ_ENERGY_II	7.48E+01	2	3.74E+01	6.02E+03	0.000
CZ_PEAK_TRAC_I	4.61E-01	2	2.30E-01	3.71E+01	0.000
CZ_PEAK_TRAC_II	1.95E+01	2	9.73E+00	1.56E+03	0.000
FRICTION_COEF	8.04E+01	2	4.02E+01	6.46E+03	0.000
Error	3.23E+01	5200	6.22E-03		
Total	4.33E+03	5304			

Table C-3: LVI load at first failure

Source	Sum Sq.	d.f.	Mean Sq.	F	Prob>F
E11	5.97E+05	2	2.99E+05	8.49E+01	0.000
E22	6.22E+07	2	3.11E+07	8.84E+03	0.000
E33	1.98E+05	2	9.91E+04	2.82E+01	0.000
NU12	3.83E+06	2	1.92E+06	5.45E+02	0.000
NU23	1.78E+05	2	8.92E+04	2.54E+01	0.000
NU13	2.60E+04	2	1.30E+04	3.69E+00	0.025
G13	2.77E+06	2	1.39E+06	3.94E+02	0.000
G23	7.33E+05	2	3.66E+05	1.04E+02	0.000
G12	1.24E+06	2	6.18E+05	1.76E+02	0.000
TENSILE_FIBER_STRENGTH_11	5.34E+01	2	2.67E+01	7.59E-03	0.992
TENSILE_FIBER_STRENGTH_22	5.31E+01	2	2.65E+01	7.54E-03	0.993
TENSILE_FIBER_STRENGTH_33	5.39E+01	2	2.69E+01	7.65E-03	0.992
TENSILE_MATRIX_STRENGTH_33	7.69E+01	2	3.85E+01	1.09E-02	0.989
COMPRESSIVE_FIBER_STRENGTH_11	6.42E+01	2	3.21E+01	9.13E-03	0.991
COMPRESSIVE_FIBER_STRENGTH_22	2.39E+04	2	1.20E+04	3.40E+00	0.033
COMPRESSIVE_FIBER_STRENGTH_33	5.38E+01	2	2.69E+01	7.65E-03	0.992
COMPRESSIVE_MATRIX_STRENGTH_33	1.94E+05	2	9.71E+04	2.76E+01	0.000
SHEAR_FIBER_STRENGTH_12	5.35E+01	2	2.67E+01	7.60E-03	0.992
SHEAR_FIBER_STRENGTH_23	5.39E+01	2	2.70E+01	7.66E-03	0.992
SHEAR_FIBER_STRENGTH_13	5.35E+01	2	2.68E+01	7.60E-03	0.992
SHEAR_MATRIX_STRENGTH_12	9.18E+01	2	4.59E+01	1.30E-02	0.987
SHEAR_MATRIX_STRENGTH_23	1.84E+04	2	9.18E+03	2.61E+00	0.074
SHEAR_MATRIX_STRENGTH_13	5.29E+01	2	2.65E+01	7.52E-03	0.993
TENSILE_FRACTURE_ENERGY_11	5.07E+01	2	2.54E+01	7.21E-03	0.993
TENSILE_FRACTURE_ENERGY_22	8.80E+01	2	4.40E+01	1.25E-02	0.988
TENSILE_FRACTURE_ENERGY_33	5.35E+01	2	2.67E+01	7.60E-03	0.992
COMPRESSIVE_FRACTURE_ENERGY_11	6.23E+01	2	3.11E+01	8.85E-03	0.991
COMPRESSIVE_FRACTURE_ENERGY_22	6.88E+01	2	3.44E+01	9.78E-03	0.990
COMPRESSIVE_FRACTURE_ENERGY_33	5.35E+01	2	2.67E+01	7.60E-03	0.992
SHEAR_FRACTURE_ENERGY_12	5.35E+01	2	2.67E+01	7.60E-03	0.992
SHEAR_FRACTURE_ENERGY_23	5.32E+01	2	2.66E+01	7.56E-03	0.993
SHEAR_FRACTURE_ENERGY_13	5.21E+01	2	2.61E+01	7.40E-03	0.993
TENSILE_DAMAGE_MODULUS_33	5.42E+01	2	2.71E+01	7.70E-03	0.992
COMPRESSIVE_DAMAGE_MODULUS_33	2.04E+02	2	1.02E+02	2.89E-02	0.972
SHEAR_DAMAGE_MODULUS_12	5.23E+01	2	2.62E+01	7.44E-03	0.993
SHEAR_DAMAGE_MODULUS_13	5.53E+01	2	2.76E+01	7.86E-03	0.992
SHEAR_DAMAGE_MODULUS_23	6.59E+01	2	3.30E+01	9.37E-03	0.991
HARDENING_EXPONENT_12	5.31E+01	2	2.66E+01	7.55E-03	0.993
HARDENING_EXPONENT_23	5.35E+01	2	2.67E+01	7.60E-03	0.992
HARDENING_EXPONENT_13	5.19E+01	2	2.60E+01	7.38E-03	0.993
HARDENING_EXPONENT_33	5.96E+02	2	2.98E+02	8.47E-02	0.919
MAXIMUM_COMPRESSIVE_DAMAGE_11	5.39E+01	2	2.70E+01	7.66E-03	0.992
MAXIMUM_COMPRESSIVE_DAMAGE_22	5.38E+01	2	2.69E+01	7.65E-03	0.992
MAXIMUM_COMPRESSIVE_DAMAGE_33	5.36E+01	2	2.68E+01	7.62E-03	0.992
COMPRESSION_COUPLING_FACTOR_11	5.30E+01	2	2.65E+01	7.54E-03	0.993
COMPRESSION_COUPLING_FACTOR_22	5.38E+01	2	2.69E+01	7.65E-03	0.992
COMPRESSION_COUPLING_FACTOR_33	5.31E+01	2	2.65E+01	7.54E-03	0.993
CZ_ENERGY_I	2.19E+05	2	1.09E+05	3.11E+01	0.000
CZ_ENERGY_II	2.18E+08	2	1.09E+08	3.09E+04	0.000
CZ_PEAK_TRAC_I	8.39E+05	2	4.20E+05	1.19E+02	0.000
CZ_PEAK_TRAC_II	1.71E+08	2	8.54E+07	2.43E+04	0.000
FRICTION_COEF	9.12E+07	2	4.56E+07	1.30E+04	0.000
Error	1.83E+07	5200	3.52E+03		
Total	6.71E+08	5304			

Table C-4: LVI Maximum load

Source	Sum Sq.	d.f.	Mean Sq.	F	Prob>F
E11	1.37E+06	2	6.87E+05	1.47E+02	0.000
E22	1.29E+06	2	6.43E+05	1.38E+02	0.000
E33	4.52E+04	2	2.26E+04	4.84E+00	0.008
NU12	2.22E+05	2	1.11E+05	2.38E+01	0.000
NU23	4.16E+05	2	2.08E+05	4.46E+01	0.000
NU13	4.31E+03	2	2.16E+03	4.62E-01	0.630
G13	2.58E+03	2	1.29E+03	2.76E-01	0.759
G23	3.88E+03	2	1.94E+03	4.16E-01	0.660
G12	1.72E+06	2	8.61E+05	1.84E+02	0.000
TENSILE_FIBER_STRENGTH_11	7.70E+02	2	3.85E+02	8.25E-02	0.921
TENSILE_FIBER_STRENGTH_22	2.10E+05	2	1.05E+05	2.25E+01	0.000
TENSILE_FIBER_STRENGTH_33	6.29E+02	2	3.15E+02	6.74E-02	0.935
TENSILE_MATRIX_STRENGTH_33	7.05E+02	2	3.53E+02	7.55E-02	0.927
COMPRESSIVE_FIBER_STRENGTH_11	4.60E+02	2	2.30E+02	4.93E-02	0.952
COMPRESSIVE_FIBER_STRENGTH_22	1.53E+04	2	7.64E+03	1.64E+00	0.195
COMPRESSIVE_FIBER_STRENGTH_33	6.99E+05	2	3.50E+05	7.48E+01	0.000
COMPRESSIVE_MATRIX_STRENGTH_33	4.67E+03	2	2.34E+03	5.00E-01	0.607
SHEAR_FIBER_STRENGTH_12	9.16E+01	2	4.58E+01	9.80E-03	0.990
SHEAR_FIBER_STRENGTH_23	2.51E+01	2	1.26E+01	2.69E-03	0.997
SHEAR_FIBER_STRENGTH_13	1.38E+02	2	6.92E+01	1.48E-02	0.985
SHEAR_MATRIX_STRENGTH_12	9.64E+05	2	4.82E+05	1.03E+02	0.000
SHEAR_MATRIX_STRENGTH_23	2.15E+04	2	1.07E+04	2.30E+00	0.101
SHEAR_MATRIX_STRENGTH_13	3.46E+03	2	1.73E+03	3.70E-01	0.691
TENSILE_FRACTURE_ENERGY_11	3.51E+01	2	1.75E+01	3.75E-03	0.996
TENSILE_FRACTURE_ENERGY_22	1.23E+07	2	6.16E+06	1.32E+03	0.000
TENSILE_FRACTURE_ENERGY_33	2.76E+01	2	1.38E+01	2.96E-03	0.997
COMPRESSIVE_FRACTURE_ENERGY_11	4.08E+02	2	2.04E+02	4.37E-02	0.957
COMPRESSIVE_FRACTURE_ENERGY_22	2.96E+03	2	1.48E+03	3.17E-01	0.728
COMPRESSIVE_FRACTURE_ENERGY_33	8.42E+02	2	4.21E+02	9.01E-02	0.914
SHEAR_FRACTURE_ENERGY_12	3.78E+01	2	1.89E+01	4.05E-03	0.996
SHEAR_FRACTURE_ENERGY_23	1.00E+01	2	5.01E+00	1.07E-03	0.999
SHEAR_FRACTURE_ENERGY_13	1.99E+01	2	9.93E+00	2.13E-03	0.998
TENSILE_DAMAGE_MODULUS_33	1.64E+02	2	8.21E+01	1.76E-02	0.983
COMPRESSIVE_DAMAGE_MODULUS_33	1.31E+06	2	6.56E+05	1.40E+02	0.000
SHEAR_DAMAGE_MODULUS_12	7.09E+03	2	3.55E+03	7.59E-01	0.468
SHEAR_DAMAGE_MODULUS_13	8.75E+03	2	4.38E+03	9.37E-01	0.392
SHEAR_DAMAGE_MODULUS_23	8.33E+01	2	4.16E+01	8.92E-03	0.991
HARDENING_EXPONENT_12	1.20E+04	2	6.00E+03	1.28E+00	0.277
HARDENING_EXPONENT_23	2.76E+01	2	1.38E+01	2.96E-03	0.997
HARDENING_EXPONENT_13	1.11E+02	2	5.55E+01	1.19E-02	0.988
HARDENING_EXPONENT_33	1.40E+06	2	7.01E+05	1.50E+02	0.000
MAXIMUM_COMPRESSIVE_DAMAGE_11	2.59E+01	2	1.30E+01	2.78E-03	0.997
MAXIMUM_COMPRESSIVE_DAMAGE_22	3.06E+01	2	1.53E+01	3.27E-03	0.997
MAXIMUM_COMPRESSIVE_DAMAGE_33	7.18E+04	2	3.59E+04	7.68E+00	0.000
COMPRESSION_COUPLING_FACTOR_11	2.37E+01	2	1.19E+01	2.54E-03	0.998
COMPRESSION_COUPLING_FACTOR_22	2.88E+01	2	1.44E+01	3.08E-03	0.997
COMPRESSION_COUPLING_FACTOR_33	2.36E+01	2	1.18E+01	2.53E-03	0.998
CZ_ENERGY_I	2.51E+02	2	1.25E+02	2.68E-02	0.974
CZ_ENERGY_II	9.76E+05	2	4.88E+05	1.05E+02	0.000
CZ_PEAK_TRAC_I	1.20E+03	2	6.02E+02	1.29E-01	0.879
CZ_PEAK_TRAC_II	7.15E+05	2	3.57E+05	7.65E+01	0.000
FRICTION_COEF	2.99E+06	2	1.50E+06	3.20E+02	0.000
Error	2.43E+07	5200	4.67E+03		
Total	8.22E+07	5304			

APPENDIX D: VERIFICATION OF POST-PROCESSING STATISTICS

A Python script utilizing the scipy.stats module was developed to automatically provide all relevant statistics for model validation given sets of experimental and model outputs. This script is verified against the commercial code Minitab. The outputs for the four-point flexure softening loads are shown in and for Python and Minitab respectively. The comparable values are highlighted in green.

```
The 4PT Bend produces the following statistics:
      Test for equal variances (accept for p-value >= 0.050):
            The Levene test statistic is 3.405 and the p-value is 0.066.

      Tests for normality (accept for p-value >= 0.050):
            The Anderson-Darling test statistic for exper is 0.455 with an
                  estimated significance (p-value) of 0.150.
            The Anderson-Darling test statistic for model is 0.513 with an
                  estimated significance (p-value) of 0.150.
            The D'Agostino and Pearson's normality test statistic for the
                  model is 0.866 and the p-value is 0.648.

      Tests equal populations (accept for p-value >= 0.050):
            The t-statistic is 2.421 and the p-value is 0.016.
            The pooled standard deviation is 100.198
            The bound on the error are [221.064, 23.096]
            The percent bound on the error are [9.993, 1.044]
            If we assume unequal variances than the t-statistic is 7.109
                  and the p-value is 0.003.

      Other tests associated with non-normal data:
            The skew for experiments is 0.009
            The skew for the model is -0.058
            The skew test for the model produces a z-statistic is -0.484
                  and the p-value is 0.628.
            The Mann-Whitney rank test statistic is 198.000 and the p-value
                  is 0.010.
            The Wilcoxon rank test statistic is 2.586 and the p-value is
                  0.010.
```

Figure D-1: Python scipy.stats output for the four point flexure softening load results

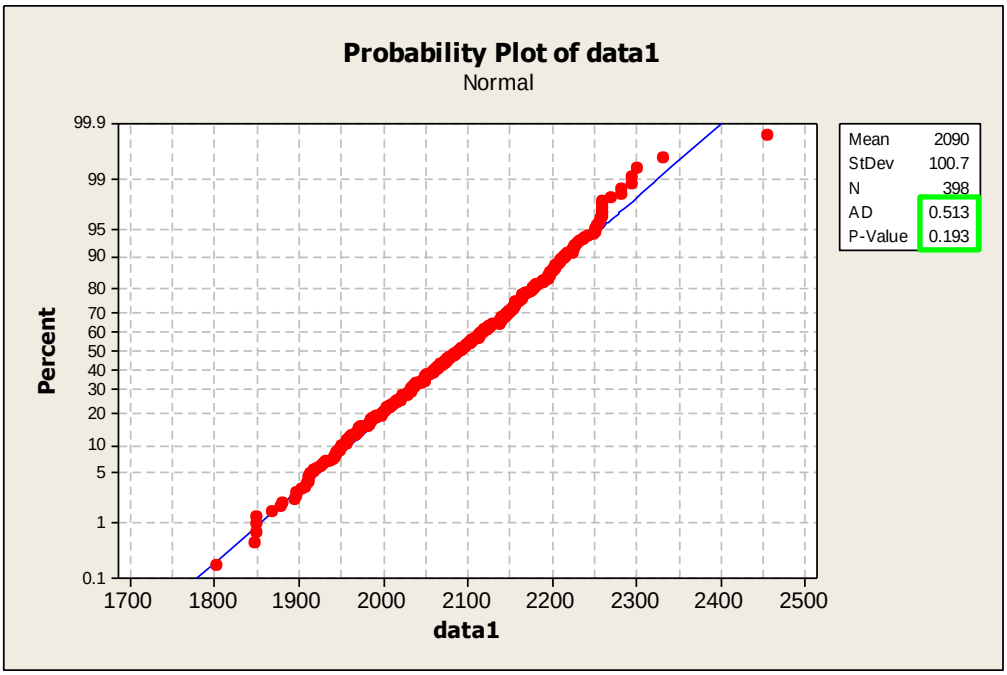

Two-Sample T-Test and CI: data1, exp

```
Two-sample T for data1 vs exp

         N    Mean  StDev  SE Mean
data1  398    2090    101      5.0
exp      4  2212.2   32.8       16


Difference = mu (data1) - mu (exp)
Estimate for difference:  -122.1
95% CI for difference:  (-221.2, -23.0)
T-Test of difference = 0 (vs not =): T-Value = -2.42  P-Value = 0.016  DF = 400
Both use Pooled StDev = 100.3327
```

Mann-Whitney Test and CI: data1, exp

```
         N  Median
data1  398  2092.5
exp      4  2211.7


Point estimate for ETA1-ETA2 is -119.6
95.0 Percent CI for ETA1-ETA2 is (-208.8,-34.6)
W = 79599.0
Test of ETA1 = ETA2 vs ETA1 not = ETA2 is significant at 0.0098
The test is significant at 0.0098 (adjusted for ties)
```

Figure D-2: Minitab output for the four point flexure softening load results

DISTRIBUTION

MS0557	D. Epp	1522 (electronic copy)
MS9035	P. Spence	8250 (electronic copy)
MS9042	M. Chiesa	8259 (electronic copy)
MS9042	J. Dike	8259 (electronic copy)
MS9042	N. Spencer	8259 (electronic copy)
MS9106	D. Gehmlich	8226 (electronic copy)
MS9106	S. Stieper	8226 (electronic copy)
MS9153	T. Shepodd	8220 (electronic copy)
MS9154	N. Bhutani	8248 (electronic copy)
MS0899	Technical Library	9536 (electronic copy)


Sandia National Laboratories